

CANDU Fuel Element Model Development and Sensitivity Study

NWMO TR-2010-12

June 2010

Adrian Popescu and Timothy Lampman

AMEC NSS Limited

nwmo

NUCLEAR WASTE
MANAGEMENT
ORGANIZATION

SOCIÉTÉ DE GESTION
DES DÉCHETS
NUCLÉAIRES



Nuclear Waste Management Organization
22 St. Clair Avenue East, 6th Floor
Toronto, Ontario
M4T 2S3
Canada

Tel: 416-934-9814
Web: www.nwmo.ca

CANDU Fuel Element Model Development and Sensitivity Study

NWMO TR-2010-12

June 2010

Adrian Popescu and Timothy Lampman
AMEC NSS Limited

Disclaimer:

This report does not necessarily reflect the views or position of the Nuclear Waste Management Organization, its directors, officers, employees and agents (the "NWMO") and unless otherwise specifically stated, is made available to the public by the NWMO for information only. The contents of this report reflect the views of the author(s) who are solely responsible for the text and its conclusions as well as the accuracy of any data used in its creation. The NWMO does not make any warranty, express or implied, or assume any legal liability or responsibility for the accuracy, completeness, or usefulness of any information disclosed, or represent that the use of any information would not infringe privately owned rights. Any reference to a specific commercial product, process or service by trade name, trademark, manufacturer, or otherwise, does not constitute or imply its endorsement, recommendation, or preference by NWMO.

ABSTRACT

Title: CANDU Fuel Element Model Development and Sensitivity Study
Report No.: NWMO TR-2010-12
Author(s): Adrian Popescu and Timothy Lampman
Company: AMEC NSS Limited
Date: June 2010

Abstract

This report documents continued work on the Bundle Stress Model for CANDU fuel. New modified models with improved pellet-to-sheath and pellet-to-pellet interactions were developed to evaluate stress fields present in spent fuel during dry storage and to calculate the stress intensity factors at the endcap-to-endplate welds.

The models were compared against a new series of validation experiments using unirradiated fuel elements. Comparison of the modelled and experimental results shows a good agreement and demonstrates that the model is capable of predicting the mechanical behaviour of the 28- and 37-element fuel bundles.

Sensitivity studies confirmed the model capability to simulate bundles with dimensions and material properties within the known variability of their values.

TABLE OF CONTENTS

	<u>Page</u>
ABSTRACT	v
1. Introduction.....	1
2. Fuel Element Models	2
2.1 Pipe Finite Element Model.....	2
2.2 Pellet-to-Sheath and Pellet-to-Pellet Interaction Finite Element Model.....	3
2.2.1 Endcap	5
2.2.2 Sheath	5
2.2.3 Sheath-to-endcap weld	5
2.2.4 Pellet.....	6
2.2.5 Pellet-to-sheath interaction	7
2.2.6 Pellet-to-pellet interaction.....	10
2.2.7 Bearing pads and spacer pads.....	10
3. Fuel Element Validation Experiments	12
3.1 Experimental Apparatus and Procedure	12
3.2 Experimental Data Analysis	14
3.3 Verification of Experimental Apparatus	16
3.4 Single Element Validation Results.....	23
3.4.1 28-Element Fuel Elements.....	23
3.4.2 37-Element Fuel Elements.....	25
4. Fuel Element Model Validation	29
4.1 Validation of 28-Element Model against Single Element Tests	29
4.2 Validation of 37-Element Model against Single Element Tests	39
5. Uncertainty and Sensitivity Studies	46
5.1 Uncertainty Parameter List	46
5.1.1 Material properties	46
5.1.1.1 <u>Young's modulus for the sheath</u>	46
5.1.1.2 <u>Cold work of sheath</u>	47
5.1.1.3 <u>Anisotropy of sheath elastic properties</u>	47
5.1.1.4 <u>Poisson's coefficient of sheath</u>	47
5.1.1.5 <u>Pre-stress of the fuel bundle</u>	48
5.1.2 Bundle design parameters	48
5.1.3 Other model parameters	50
5.1.3.1 <u>Finite element sizes</u>	50
5.1.3.2 <u>Pellet-to-sheath interaction</u>	50
5.2 Analysis Methodology.....	50
5.3 Uncertainty Analysis for 28-Element Bundle Model.....	51
5.4 28-Element Model Sensitivity to Axial Size of the Finite Elements	55
5.5 Uncertainty Analysis for 37-Element Bundle Model.....	57
5.6 Bundle Model Sensitivity to Circumferential Size of the Finite Elements....	60

6.	Conclusions	62
7.	References	63

LIST OF TABLES

	<u>Page</u>
Table 1: Model Components of Fuel Element with Pellets.....	4
Table 2: Solid Rod Verification Analysis Results	20
Table 3: Material Property Best Estimate Values and Uncertainties.....	48
Table 4: Design Parameters Best Estimate Values and Uncertainties.....	49
Table 5: Confidence Level as a Function of Number of Samples to have 95% of the Population between First Minimum and First Maximum of All Samples	51
Table 6: Best Estimate Values and Uncertainty used for 28-Element Bundle Sensitivity Analyses.....	52
Table 7: Best Estimate Values and Uncertainties used for 37-Element Bundle Sensitivity Analyses.....	58

LIST OF FIGURES

	<u>Page</u>
Figure 1: Pipe FE Model of the Fuel Element.....	3
Figure 2: 28-Element Endcap Finite Element Model	5
Figure 3: Sheath Finite Element Model	5
Figure 4: Sheath-to-Endcap Weld Finite Element Model	6
Figure 5: Pellet Finite Element Model.....	6
Figure 6: Local Coordinate System for INTER195 Finite Element	7
Figure 7: Pellet-to-Sheath Interface Model	7
Figure 8: Comparison of Physical and Modelled Pellet-to-Sheath Interface	8
Figure 9: Material properties used for pellet-to-sheath interfaces.	9
Figure 10: Bearing Pad Brazed on the Sheath Surface	10
Figure 11: Modified Experimental Apparatus for Single Elements	12
Figure 12: Schematic Diagram of the Solid Rod Experimental Setup	13
Figure 13: Experimental Element Loading Fixtures	13
Figure 14: Fuel Element Experimental Clamps	14
Figure 15: Time Series Plot of Solid Rod Test.....	15
Figure 16: Analysis of LVDT Displacement Prior to Load Cycle	15
Figure 17: Analysis of Load Cell Signal at Maximum Displacement of Load Cycle	16
Figure 18: Solid Rod Response Measured at Middle LVDT.....	17
Figure 19: Solid Rod Response Measured at Inner LVDTs	18
Figure 20: Solid Rod Response Measured at Outer LVDTs	19
Figure 21: Analytic Equations used for Off-Center 3-Point Bending	19
Figure 22: ANSYS Finite Element Model used for Solid Rod Validation Test Modelling	20
Figure 23: Solid Rod Finite Element Model von Mises Stress Field under Loading	21
Figure 24: Solid Rod Experimental and Calculated Middle LVDT Responses	21
Figure 25: Solid Rod Experimental and Calculated Inner LVDT Responses.....	22
Figure 26: Solid Rod Experimental and Calculated Outer LVDT Responses.....	23
Figure 27: 28-Element Response Measured at Middle LVDT	24
Figure 28: 28-Element Response Measured at Inner LVDTs	25
Figure 29: 28-Element Response Measure at Outer LVDTs.....	26
Figure 30: Comparison of 28-Element Full-Bundle and Single-Element Test Results	26
Figure 31: 37-Element Response Measured at Middle LVDT.....	27
Figure 32: 37-Element Response Measured at Inner LVDTs	27

Figure 33: 37-Element Response Measured at Outer LVDTs.....	28
Figure 34: Comparison of 37-Element Full-Bundle and Single-Element Test Results	28
Figure 35: Non-Axial Load Test Simulation Boundary Conditions and Geometry	29
Figure 36: Measured and Modelled Response of 28-Element Fuel Element	30
Figure 37: Analytical Cases Describing (a) Fixed Beam and (b) Simply Supported Beam.....	31
Figure 38: Comparison of Responses of the 28-Element Fuel Element	31
Figure 39: Equivalent Stress in the 28-Element Endplate for 2 mm Deformation.....	32
Figure 40: Equivalent Stress in the 28-Element Endplate for 12.5 mm Deformation.....	33
Figure 41: Equivalent Strain in the 28-Element Endplate for 12.5 mm Deformation	33
Figure 42: Equivalent Stress in 28-Element Sheath for 12.5 mm Deformation	34
Figure 43: Pellet-to-Sheath Interface Closure for 28-Element Model with 12.5 mm Deformation	35
Figure 44: Pellet-to-Sheath Interface Closure for 28-Element Model with 8 mm Deformation....	35
Figure 45: Pellet-to-Sheath Interface Closure for 28-Element Model with 6 mm Deformation....	36
Figure 46: Average Pellet-to-Sheath Pressure vs. 28-Element Deformation	36
Figure 47: Equivalent Stress in Pellets for 28-Element Model with 8 mm Deformation	37
Figure 48: Equivalent Stress in Pellets for 28-Element Model with 4 mm Deformation	38
Figure 49: Pellet-to-Pellet Contact Pressure for 28-Element Model with 8 mm Deformation.....	38
Figure 50: Pellet Interaction of 28-Element Model for 12.5 mm Deformation (10x Scale).....	39
Figure 51: Measured and Modelled Response of a 37-Element Fuel Element	40
Figure 52: Equivalent Stress in 37-Element Endplate for 16.5 mm Deformation.....	41
Figure 53: Equivalent Stress in 37-Element Sheath for 16.5 mm Deformation	42
Figure 54: Pellet-to-Sheath Interface Closure for 37-Element Model with 16.5 mm Deformation	43
Figure 55: Pellet-to-Sheath Interface Closure for 37-Element Model with 10 mm Deformation	43
Figure 56: Pellet-to-Sheath Interface Closure for 37-Element Model with 7.5 mm Deformation	44
Figure 57: Average Pellet-to-Sheath Pressure vs. 37-Element Deformation	44
Figure 58: Equivalent Stress in Pellets for 37-Element Model with 10 mm Deformation	45
Figure 59: Pellet Interaction for 37-Element Model with 12.5 mm Deformation (10x Scale).....	45
Figure 60: 28-Element Bundle Model Predictions for GRS Matrix Cases	53
Figure 61: Influence of the Pellet-to-Pellet Axial Gap on the 28-Element Fuel Bundle Model Predictions	54
Figure 62: Influence of the Zircaloy-4 Elastic Modulus on the 28-Element Fuel Bundle Model Predictions for 2 mm Load Case	54
Figure 63: Influence of the Pellet-to-Pellet Axial Gap on the 28-Element Fuel Bundle Model Predictions for 6 mm Load Case	55
Figure 64: Comparison of Sheath Mesh for Axial Mesh Size Sensitivity Analysis	56
Figure 65: Results of Axial Mesh Size Sensitivity Study	56
Figure 66: 37-Element Bundle Model Predictions for GRS Sensitivity Cases	59
Figure 67: Influence of the Pellet-to-Pellet Axial Gap on the 37-Element Fuel Bundle Model Predictions	59
Figure 68: Influence of the Zircaloy-4 Elastic Modulus on the 37-Element Fuel Bundle Model Predictions for 2.5 mm Deflection Case	60
Figure 69: Sensitivity Study for Finer Mesh in Circumferential Direction.....	61
Figure 70: Sensitivity Study for the Circumferential Size of Finite Elements	61

1. INTRODUCTION

Previous analysis performed by AMEC NSS indicated that Delayed Hydride Cracking (DHC) could be a potential degradation mechanism affecting the integrity of used fuel bundles stored in dry conditions such as in Dry Storage Containers (DSC) (Lampman & Daniels, 2005). The endcap-to-endplate welds were identified as an area of concern due to post-manufacturing weld geometries. The risk of DHC in the welds is related to the stress levels present in the weld region during dry storage. To evaluate the stress levels present in storage, a stress model of the fuel bundle was proposed by NSS to assess whether DHC could occur in bundles stored in dry storage conditions.

During 2006 and 2007, NSS developed parametric ANSYS Finite Element (FE) models of commercial 28- and 37-element CANDU fuel bundles (Lampman, 2008). The models account for bowing deformations of the fuel elements resulting from their in-reactor service life. Results obtained with the bundle stress model were verified against test results performed on non-irradiated fuel bundles at Stern Laboratories.

In general, reasonable agreement between the model predictions and the test results was achieved. However, the models overpredicted displacements of the bundle elements and underpredicted displacements of the endplates. As a result, further work was pursued to resolve the causes leading to the differences.

In achieving this objective, modifications were made to the fuel element models to improve the pellet and sheath interaction. Another series of validation tests were also performed with a simplified single-element geometry. To examine the accuracy of the experimental apparatus, three-point loading tests on solid rods with the same equipment used previously but slightly modified to allow for testing of the rods and single fuel elements were performed. Comparison of test results with the new fuel element models was made. A detailed discussion is provided in Sections 3 and 4.

The current models for the 28- and 37-element fuel bundles predict accurately the deformation of the fuel elements when loaded normally at the mid-point along the element length. Sensitivity studies with the new models were performed to explore what impact the variability on the fuel element dimensions and material properties has on the model results. Details of this effort are provided in Section 5. The sensitivity studies for the fuel bundle models demonstrate that they can be successfully applied within the known variability of the design parameters and material properties.

2. FUEL ELEMENT MODELS

New finite element models have been created for the individual fuel elements for both 28- and 37-element fuel bundles. The models were created to improve the accuracy of the initial fuel bundle FE models (Lampman, 2008) in comparison with the validation tests. The FE models were also modified to help improve the convergence of the ANSYS solutions and decrease the solution time and memory requirements. Two basic fuel element models were created: a simple fuel element using pipe finite elements that does not model the fuel pellets; and a finer meshed fuel element with the pellets-to-sheath interaction simulated with a specialized interface finite element, commonly used in ANSYS to model gaskets. The first model is used to represent the rigidity and weight of the fuel elements in regions of the bundle remote from the analysis region. The second model is an explicit model of the interactions of the pellets and sheath and is used directly in the analysis regions.

2.1 Pipe Finite Element Model

The pipe finite element model was developed for simulation of fuel elements that are not close to the area of interest in the simulation. They greatly reduce the size of the model, thus decreasing solution times, while maintaining the general structural rigidity of the fuel bundle. The fuel bundle model ANSYS Parametric Design Language (APDL) input scripts have been modified to allow the user to select which fuel element model to be used for each individual element. Therefore, elements in the fuel bundle remote from the area of interest can be selected to be simpler pipe FE models.

The pipe FEs are 2-node, 3D elements with density and rigidity accounted for in the FE. The inner and outer radii of the FEs are applied through FE parameters. The pipe element model is only used to model the mechanical behaviour of the fuel sheath and pellets are not modelled. The fuel element appendages (bearing pads and spacer pads) have not been incorporated into the model, but can be added as necessary to the model to capture the effects of contacts between adjacent spacers. The density of the fuel pellets has been incorporated into the sheath density to reproduce the proper weight of the fuel element. The endcaps of the fuel element are modelled with brick FEs identical to the hollow and contact fuel element models (Lampman, 2008) and are coupled to the pipe FEs.

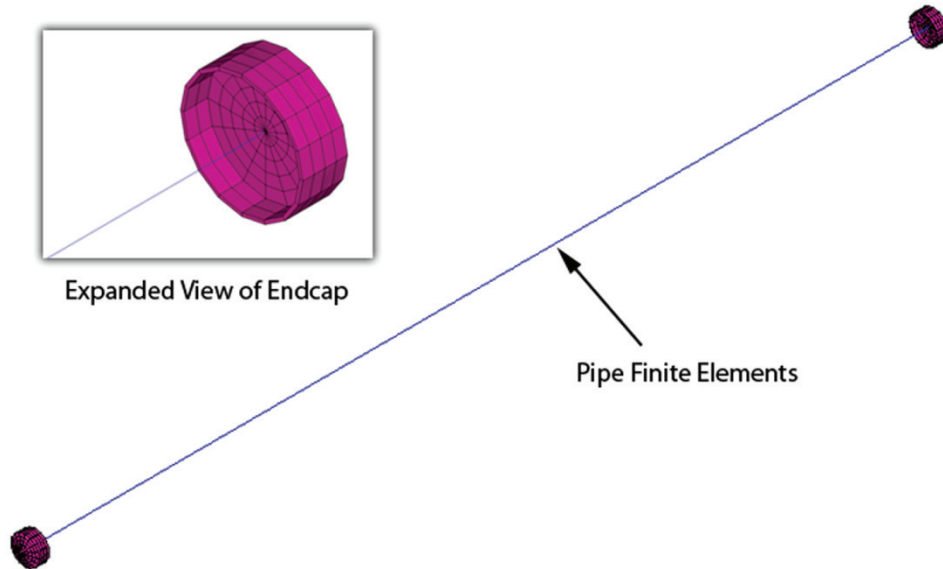


Figure 1: Pipe FE Model of the Fuel Element

A single pipe FE model is shown in Figure 1. The pipe elements representing the sheath and pellets are “line” finite elements connected to the central interior nodes of the endcaps. Translational degrees of freedom (DOF) for the pipe nodes are sufficient to translate the bending moments of the sheath to the endcaps. In order to suppress fuel element rotations relative to the face of the endcap, the pipe finite elements are overlapped with the endcap along an axial length equal to the length of the endcap plug. This approximation is consistent with the intended usage of the model; *i.e.*, for fuel elements that are not directly subjected to external loads. The small overlap of approximately 2.6 mm between the endcap and the sheath is not deemed to affect the stress and strain predictions since the sheath is very thin compared to the bulk material of the endcap.

The pipe FE fuel element model is greatly simplified from the explicit contact models and leads to smaller models and quicker solution times. The response of the pipe fuel element model is also very similar to the explicit models. However, modelling of fuel element appendages and their contacts with neighbouring elements cannot be implemented and the distribution of stress through the sheath and/or pellets is not possible with this model. At larger deflections, the pipe models are expected to deviate from the explicit contact models because pellet effects on the fuel element stiffness are not accounted for in the pipe model. Therefore, this fuel element model will only be used for elements external to regions of interest in the fuel bundles.

2.2 Pellet-to-Sheath and Pellet-to-Pellet Interaction Finite Element Model

Recent mechanical tests performed on fuel elements showed that for high loads applied non-axially, the measured response (force vs displacement) presents a stiffening effect that increases with the applied load (Snell, 2009). For an as-received bundle in the absence of mechanical deformations the pellets’ interactions with the sheath and neighbour pellets are relatively small due to the presence of radial and axial gaps. At low non-axial deformations the fuel element response is dictated by the mechanical response of the bundle’s structural components (sheath, endcaps, and endplates) since the pellet interactions remain negligible. However, the stiffening seen in the experiments appears to be controlled by the interactions between adjacent pellets and contact of the pellets with the sheath for high non-axial

deformations. The bending of the fuel element leads to changes in the sheath diameter and cross section (ovality) which affects the diametral clearance, or radial gap, between the pellets and the sheath, as well as pellet-to-pellet clearances, or axial gaps. Closure of radial and axial gaps induced by the sheath deformation will increase the stiffness of the fuel element assembly with a contribution from the significantly stiffer UO₂ pellets.

A finite element model for the fuel element was developed to evaluate the pellet-to-sheath and pellet-to-pellet mechanical interactions. The key aspect of the new fuel element model is the use of a specialized interface finite element (INTER195 in ANSYS library) to simulate the pellet-to-sheath interaction. This fuel element model can be used to simulate any fuel element in a 28- or 37-element fuel bundle.

Table 1 summarizes the components of the fuel element model and lists the finite element type, according to ANSYS library of finite elements, and the material for each component. The bundle endplates and the welds between endplates and endcaps remain unchanged from the previously developed finite element models (Lampman, 2008).

The design parameters defining the fuel element model remain unchanged from the previously developed finite element models (Lampman, 2008). Similarly, the elasto-plastic material properties for Zircaloy-4 and UO₂ of the new model are the same as the previously developed model (Lampman, 2008). Therefore, the new fuel element model is compatible with the full-bundle model. However, because some of the design parameters and material properties were identified as potential uncertainty parameters, an additional set of parameters have been added to allow for their modification during the sensitivity studies.

The following sections describe the fuel element components in more detail.

Table 1: Model Components of Fuel Element with Pellets

Component	Finite element	Material
Endcap	SOLID45	Zircaloy-4
Sheath	SHELL143	Zircaloy-4
Sheath/endcap weld	TARGE170/CONTA175 (node-to-surface contacts using MPC algorithm, always bonded)	N/A
Pellet	SOLID45	UO ₂
Pellet/sheath interaction	INTER195	Contact interface material properties
Pellet/pellet interaction	TARGE170/CONTA173 (surface-to-surface contacts using augmented Lagrange algorithm)	N/A
Bearing pad	SOLID45	Zircaloy-4
Spacer	SOLID45	Zircaloy-4
Bearing pads or spacers/sheath brazing	TARGE170/CONTA175 (node-to-surface contacts using augmented Lagrange algorithm, always bonded)	N/A

2.2.1 Endcap

The endcap of the fuel element is similar to the endcap used in the previously developed fuel element models (Lampman, 2008). The endcap is simulated using 3D solid finite elements (SOLID45) and is coupled with the fuel bundle endplate using common nodes and coupled with the sheath using contacts. The FE mesh presents cylindrical symmetry with a total of 16 arcs used for the circumference, as shown in Figure 2 for the endcap of 28-element bundle.

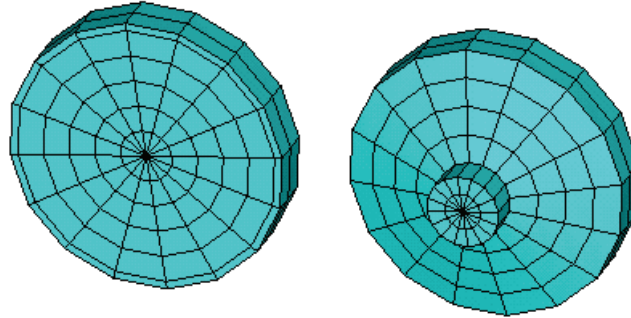


Figure 2: 28-Element Endcap Finite Element Model

2.2.2 Sheath

The cylindrical sheath was modelled using shell finite elements (SHELL143). The finite elements are located at the middle of the actual sheath thickness and the sheath thickness is incorporated directly in the FE. In the circumferential direction, a total of 16 finite elements were used to match the endcap. In the axial direction, the number of finite elements is user specified, but the mesh is created so the node locations of the sheath align with the nodes located on the pellets' surface. At both ends of the sheath, the axial gap between the pellets and the endcaps is modelled, as shown in Figure 3, to ensure alignment of the pellet and sheath nodes.

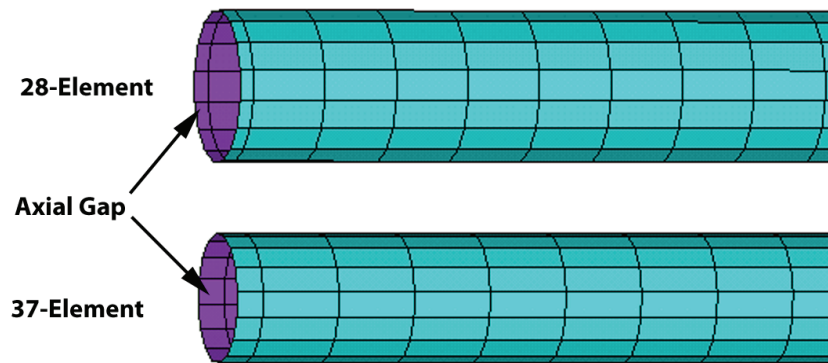


Figure 3: Sheath Finite Element Model

2.2.3 Sheath-to-endcap weld

The weld between the sheath and endcap is modelled using “always bonded” node-to-surface contacts (TARGE170 and CONTA175 element pairs). The target finite elements are placed on the inner surface of the endcap and the contact finite elements are located on all nodes at the

end of the sheath. In Figure 4 the finite element model for the welded endcap/sheath assembly is presented sectioned with a plane that passes through the fuel element centreline.

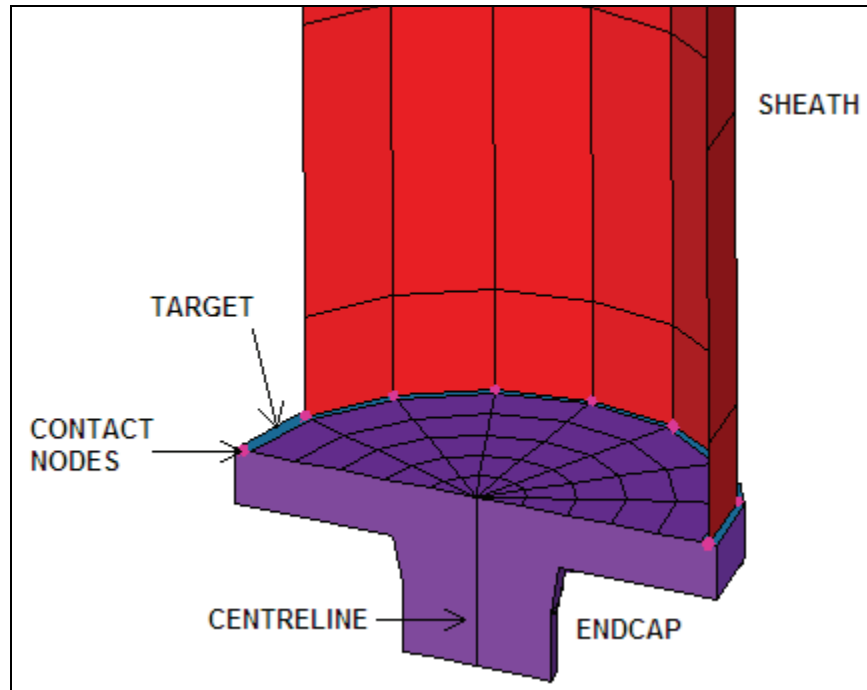


Figure 4: Sheath-to-Endcap Weld Finite Element Model

2.2.4 Pellet

Each pellet is modelled as a cylinder using 3D solid finite elements (SOLID45). In the circumferential direction the pellets are modelled using 16 arc segments, shown in Figure 5, to match the sheath. The number of finite elements in the longitudinal direction can be established using a model parameter, but a minimum of 2 finite element planes per pellet is required. Initially, prior to deformation, the nodes of the pellet exterior surface are aligned with the sheath nodes by matching the same axial and angular locations. As the fuel element deforms, nodes of the sheath and pellets move in response to the applied force and the alignment is not maintained.

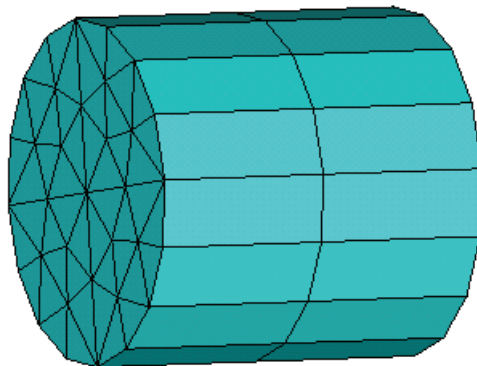


Figure 5: Pellet Finite Element Model

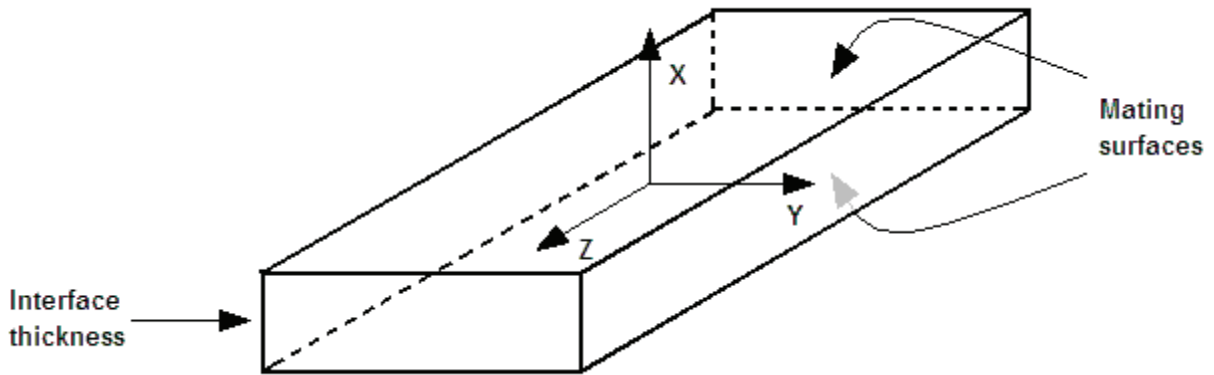


Figure 6: Local Coordinate System for INTER195 Finite Element

2.2.5 Pellet-to-sheath interaction

Different modelling solutions were tested to simulate the interaction between pellets and sheath. Models based on contact finite elements overlaid on the inner surface of the sheath and on the pellet surface were found to work correctly for a limited range of loads. A more robust solution was found using a specialized type of finite element, INTER195, recommended for simulation of 3D interfaces. The finite element is a parallelepiped defined by 8 nodes with the capability to simulate the interface between two opposite faces perpendicular to the finite element local x-axis (see Figure 6).

From the mechanical point of view, INTER195 finite element transmits forces (in terms of pressure) between two mating surfaces. In the current implementation the mating surfaces are the fuel pellet outer surface and the sheath mid-thickness surface. The value of the pressure applied on the mating surfaces is a function of the interface thickness (shown in Figure 6) and the material properties declared for this element. For most of the applications the material properties under compression for INTER195 can exhibit high nonlinearities and this can be used to simulate contact between the mating surfaces.

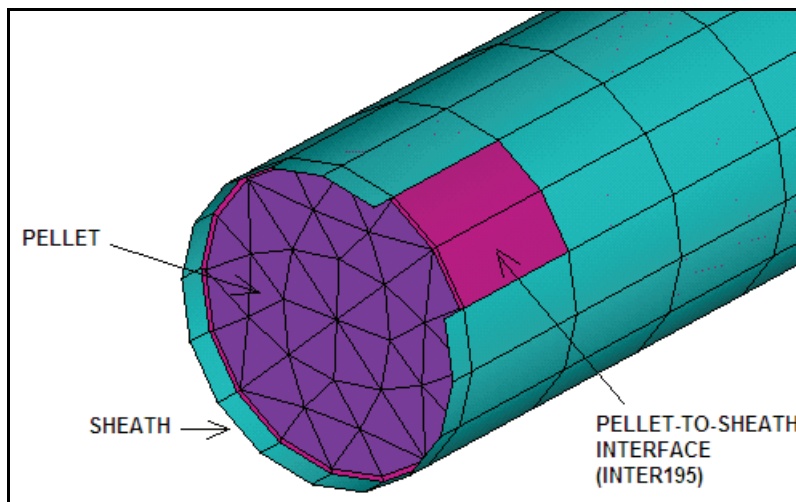


Figure 7: Pellet-to-Sheath Interface Model

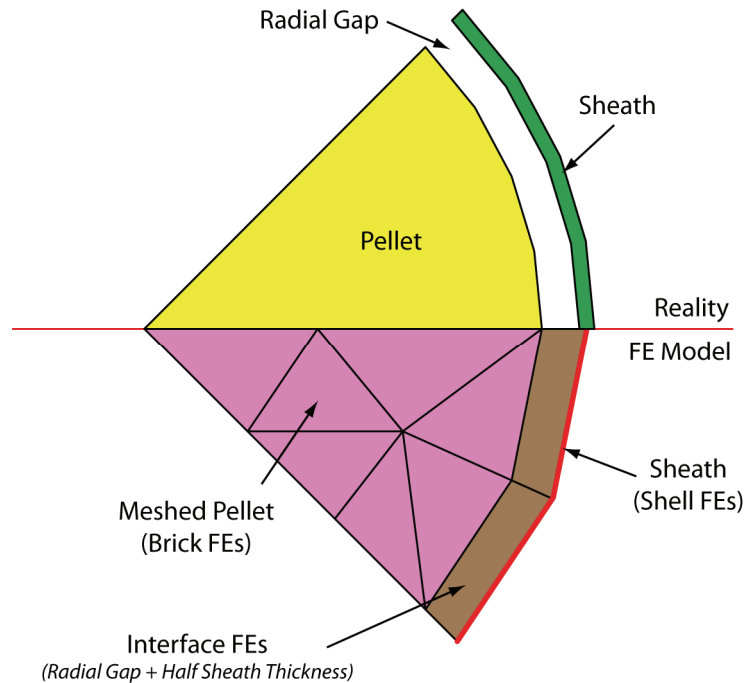


Figure 8: Comparison of Physical and Modelled Pellet-to-Sheath Interface

Geometrically, the INTER195 finite elements representing the pellet-to-sheath interface were placed between the pellet surface and the shell finite elements used to simulate the sheath, Figure 7. Because the nodes from the fuel pellet surface and the sheath nodes are aligned in axial and circumferential directions, the construction of interface finite elements is based on neighbour nodes of both surfaces. The finite element local x-axis was aligned with the fuel element radial axis for all interface elements created. Since the sheath is modelled using shells, the thickness of the interface is equal to the radial sheath-to-pellet gap plus half the thickness of the sheath, as shown in Figure 8.

The material properties of the interface were developed to simulate mechanical contact behaviour between two surfaces. In the idealized case, as shown in Figure 9, there is no pressure between surfaces until they come into contact (interface closure¹ equals the radial gap) and the pressure steps up to the contact equilibrium pressure. The finite element contact pair approach used in previous pellet models applied a methodology very similar to this, but the discontinuity in the pressure led to convergence problems. The interface finite element approach alleviates the convergence problems by smoothing the transition of mechanical contact, as shown in Figure 9.

With the interface element there is no pressure applied to the surfaces for small closures of the interface. As the closure exceeds the radial gap distance, the pressure increases rapidly to simulate mechanical contact. The radial gap in Figure 9 is the nominal design gap of 0.04 mm, and this represents the first point where the interface pressure is non-zero. The pressure required for equilibrium is unknown, but from analyses it was established that the interface pressure, *i.e.* the stress normal to the mid-surface of the interface, peaked at values around

¹ The closure of the interface is defined as the separation between the mating surfaces relative to the initial thickness of the interface. As the two surfaces move towards each other, the closure increases, and *vice-versa* when the surfaces move farther apart.

8 MPa for high non-axial loads. Therefore, equilibrium is achieved at small pressures. However, the finite element solver requires higher pressures to reach equilibrium and this is why the material property curve has been extended to higher deformation and pressure.

The ability to define the material properties and radial gap through the interface is an important feature of the current model for pellet-to-sheath interaction. It allows the inclusion of other factors affecting pellet-to-sheath contact, such as surface roughness the definition of the interface material properties. Instead of changing the pellets or sheath diameters to simulate different gaps during sensitivity studies, the radial gap can be efficiently modified by shifting the material property curve.

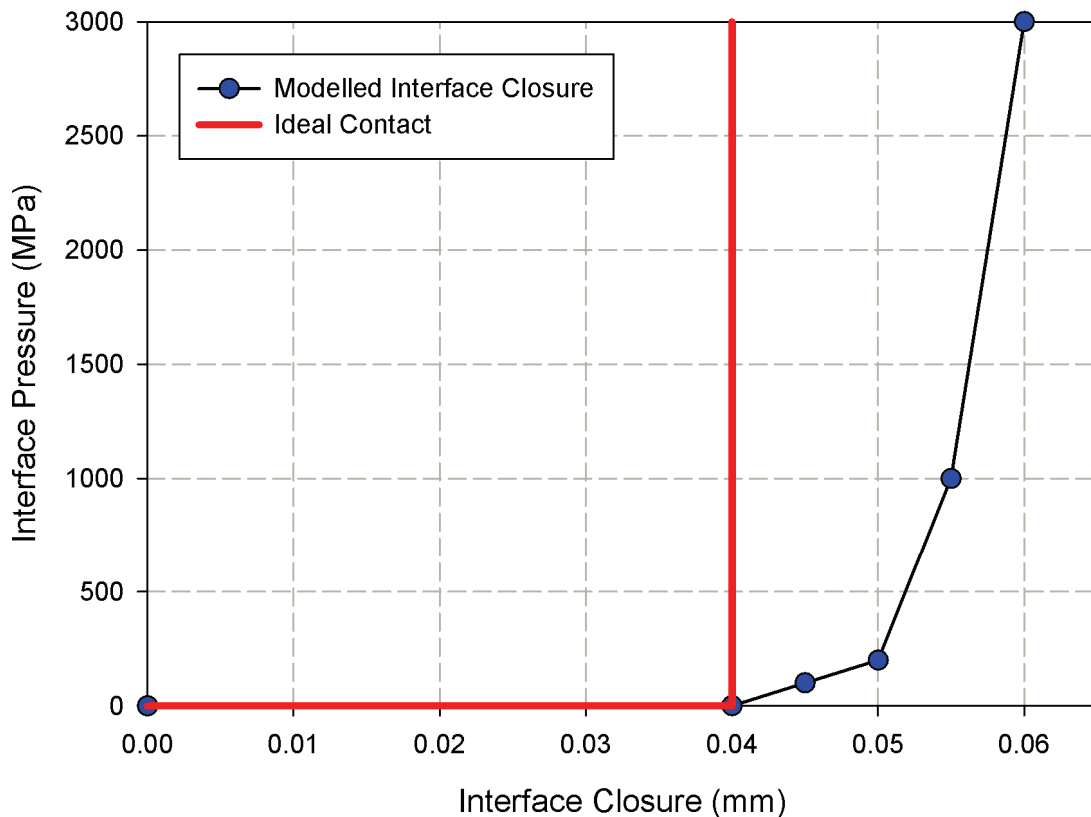


Figure 9: Material properties used for pellet-to-sheath interfaces.

The material property of the interface presented in Figure 9 relates the normal pressure between the sheath and the pellet with the distance between them and does not account for frictional forces between the pellets and the sheath. Modeling the pellet mid-plane nodes coupled with the sheath nodes in axial direction represent an approximation that is used by other fuel element behaviour computer codes. In this approximation the relative movement between the sheath and the pellets is zero at the mid-plane of the pellet. The approximation is equivalent to a high friction force between the pellets and sheath when the radial gap is closed. The friction force is concentrated at the mid-plane of the pellet. Optionally, this friction force can be distributed along the pellet surface, as a function of relative movement between pellet and sheath, if a shear modulus for the interface finite element is included in the material properties. For pellet relocation, even when the friction forces are very high, this phenomenon can still be

simulated by means of a set of input parameters used to offset the contact surfaces between the pellets.

2.2.6 Pellet-to-pellet interaction

A combination of surface contact pair finite elements (TARGE170 and CONTA173) were used to simulate the pellet-to-pellet interaction. Each contact pair is identified with a different real constant to assure the capability to model and monitor the many gaps between the pellets. The axial gap is not modelled geometrically, but set through a contact offset value declared for each contact pair.

In reality, the axial gap between pellets varies for each gap. The model is capable to simulate different gaps between each pair of pellets, but in the absence of such detailed information it is assumed that the gaps between the approximately 30 pellets in a fuel element are randomly distributed around a mean gap size. As a result, modelling the mean value of the gap is a good approximation to predict the overall mechanical response of the fuel element during bending.

2.2.7 Bearing pads and spacer pads

The fuel element bearing pads and spacers are modelled using 3D finite elements (SOLID45). In the current model, a simplified parallelepiped is used for these components. This simplification omits modelling the bevelled surface at the axial ends of bearing pads, rounded corners of spacer pads, 15° rotation angle of the spacer pads, and the curve of the top surface of the bearing pad and spacer pad which follow the curvature of the sheath. These omissions can affect the stiffness of the element, but are expected to be very minor given the localized region of the fuel element that is affected.

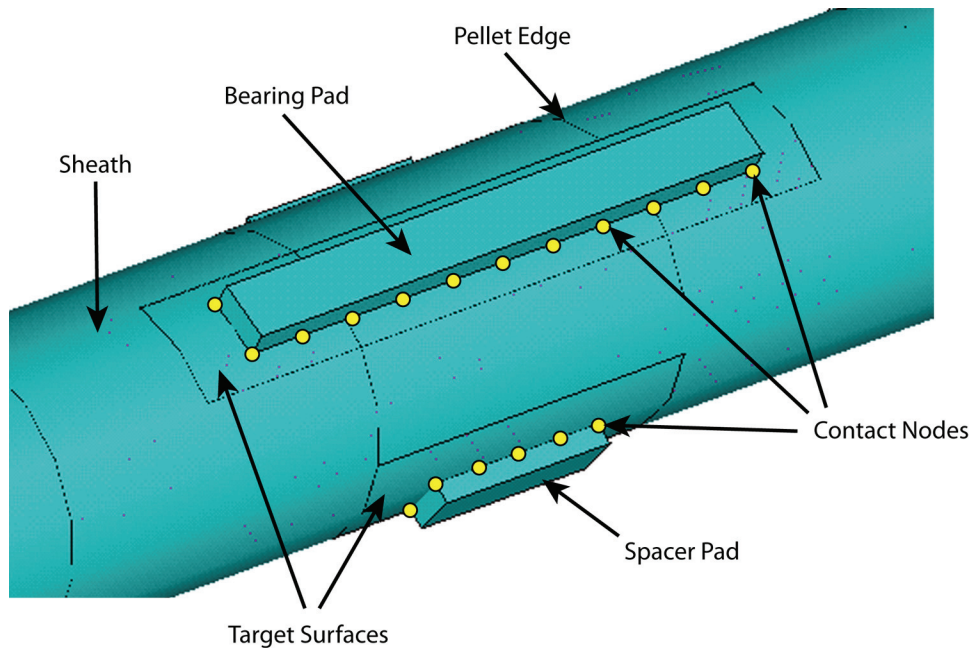


Figure 10: Bearing Pad Brazed on the Sheath Surface

Brazing of the bearing pads and spacer pads to the fuel sheath is simulated using always bounded (augmented Lagrange algorithm) node-to-surface contact pairs (TARGE170 and CONTA175 finite elements). An example of the bearing pad brazed on the fuel sheath surface is presented in Figure 10. The target surfaces are meshed on the shell finite elements of the sheath and the bearing pads are offset with half of the sheath thickness corresponding to the sheath outer surface. Spacer pads are not offset to preserve the perpendicularity of their surfaces to the element radius, given that they are not symmetrical over an edge between sheath shell elements. The nodes on the spacer pad and bearing pad surfaces closest to the sheath are used for the contact finite elements, as show in Figure 10.

3. FUEL ELEMENT VALIDATION EXPERIMENTS

Additional validation experiments were performed to better understand the mechanical response recorded during the first set of validation experiments (Lampman, 2008). The original experiments used full unirradiated fuel bundles with loads applied to elements in three manners: single element pulled radially away from bundle, single element pushed radially into the bundle, and several elements translated laterally. Constraints were applied remote from the loaded elements and the resultant deformation of the element was measured using LVDTs. The measured displacements showed significant stiffening of the elements at the higher loads used in the tests (approximately 400 N applied to a single element). The models were unable to completely account for the non-linear behaviour and some inconsistencies existed in the experimental data sets. An extension of the original experiments was performed using a simpler geometry, specifically a single fuel element removed from the bundle, and verification of the apparatus using solid rods.

3.1 Experimental Apparatus and Procedure

The experimental apparatus is nearly identical to the apparatus used for the initial full-bundle experiments (Lampman, 2008). A picture of the apparatus setup with the three-point solid rod loading configuration is shown in Figure 11. Structurally, the apparatus is nearly the same with modifications to allow for new types of constraints, additional frame supports, and relocation of the LVDTs.

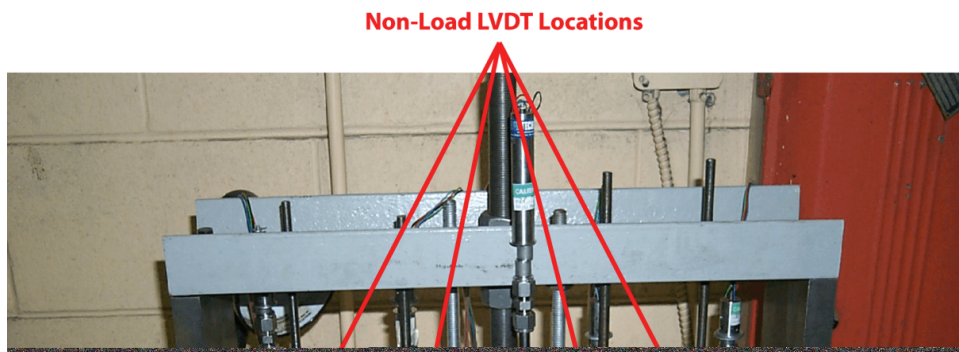


Figure 11: Modified Experimental Apparatus for Single Elements

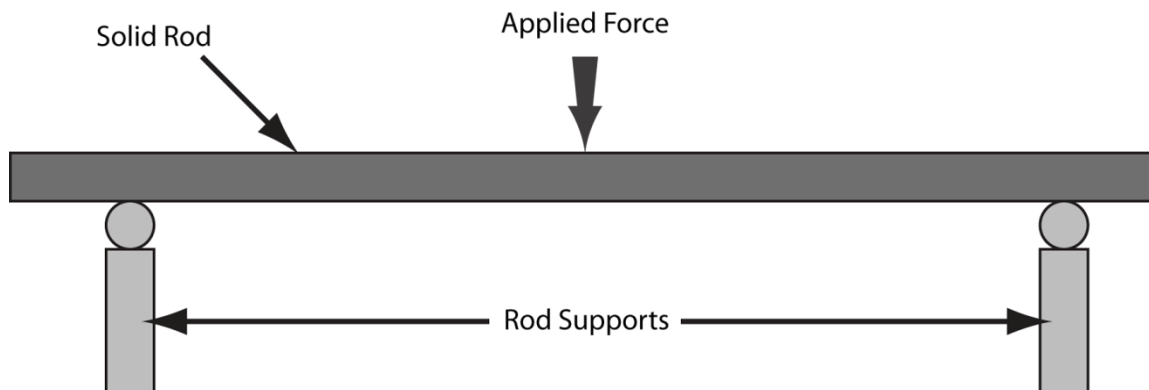
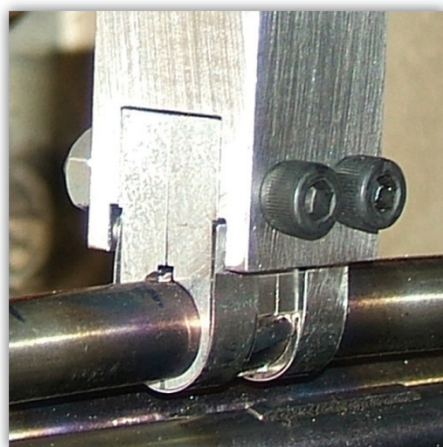


Figure 12: Schematic Diagram of the Solid Rod Experimental Setup

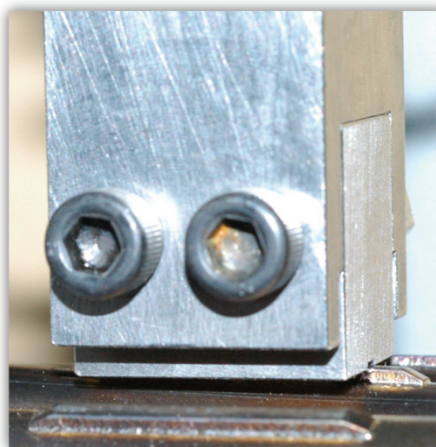
The test procedure is identical to the full bundle experiments where the loads are progressively increased by loading and unloading the test specimen (rod or fuel element) after the application of each load. All LVDT and load cell measurements are recorded by the data acquisition system at 10 Hz and saved to disk for analysis.

Modifications to the apparatus structure were made to allow the use of all 5 LVDTs to measure the deflection of the element along its axis. Previously, there were 3 LVDTs for such purpose and 2 to measure endplate deflections, but the endplate data were too uncertain and these LVDTs were used for the measurement of axial deflection. However, the LVDTs used as *inner* LDVTs (located between the *middle* LVDT where the load is applied and the *outer* LVDTs nearest the ends of the elements) had a limited range of approximately 6 mm and were frequently overranged when the higher loads were applied. Holes were also drilled into the sides of the apparatus to allow for mounting of the new single element constraint brackets.

The setup for the solid rod verification tests are shown in Figure 11 and as a schematic in Figure 12. This experiment was set up as a simple 3-point loading test with a very simple beam geometry. The rod was manufactured to the same dimensions as the fuel elements of the 37-element CANDU fuel bundle and was made of Stainless Steel 304 (SS304). Modelling of this type of experiment is straightforward and the accuracy of the apparatus could be determined.



(a) Element Pull Clamp



(b) Element Push Clamp

Figure 13: Experimental Element Loading Fixtures

However, the “element push clamp”, see Figure 13(a), was also used for providing loads to the rod in a pushing mode, *i.e.* by loading the rod downwards in the direction of gravity. The load cycles started at 100 N and were increased by 100 N increments per cycle up to a maximum load cycle of 500 N. A total of 3 tests with different rods were performed, each repeating the same experimental procedure. The LVDT measurements were compared against analytical values and modelled values from ANSYS as documented in Section 3.3.

The experimental setup for testing fuel elements from the 28- and 37-CANDU fuel bundles was nearly identical to the solid rod tests. The force was applied to the center of the element on the middle bearing pad using the *element push clamp* from the initial full-bundle experiments (shown in Figure 13). The 5 LVDTs were in approximately the same location and the load cycling was performed as before, but with a smaller increment between each load cycle. The main difference was how the constraints were applied to the single elements compared to the solid rod. A 3-point loading configuration was not used for the elements. Instead, sections of the endplates still attached to the element were clamped between two blocks to firmly constrain each end of the element. This arrangement for one end of a fuel element is shown in Figure 14. The blocks were manufactured so the endplate is not constrained 12.7 mm from the center of the assembly weld. As the element is deformed, the sheath does not contact the clamping blocks.

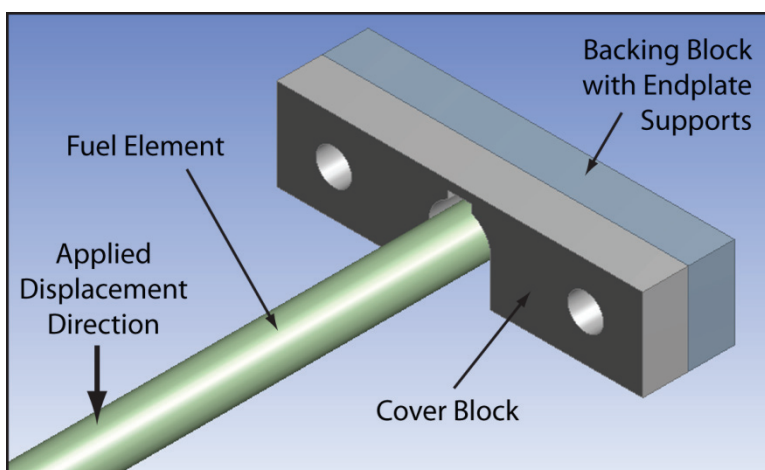


Figure 14: Fuel Element Experimental Clamps

3.2 Experimental Data Analysis

The data for each experiment is saved by the data acquisition system to Microsoft Excel files with a sampling frequency of 10 Hz. The acquisition channels containing the LVDT and load cell measurements are then selected and saved as comma separated files for analysis using MATLAB scripts. An example of the raw time-series data collected by the data acquisition system is shown in Figure 15. A total of 5 load cycles with 100 N increments for each cycle can be seen.

The time series data is not of primary interest for the analysis. Rather, the maximum loads and displacements for each cycle are of greater interest. The final displacement after the load cycle is also of interest because it indicates if plastic deformation occurred. The procedure to determine this is identical to the initial full-bundle experiments (Lampman, 2008). However, some improvements were made because of the observed time-dependent behaviour of the

measurement signals and non-zero loads at the start and end of the load cycles. Therefore, some new numerical techniques were used to determine the initial, peak, and final loads and displacements.

The initial and final loads and displacements are determined by evaluating the LVDT and load signals around the zero load points. A region of the time series including the last part of the previous load cycle, as shown in Figure 16(a), is extracted for the load and displacement signals and an XY scatter plot, as shown Figure 16(b), of the displacement versus the load is created. Since the displacement is small, a straight line can be fit to the data to determine the y-intercept. This is taken as the displacement at zero load for the particular cycle and was repeated for each LVDT signal to determine the initial and final displacements for each load cycle.

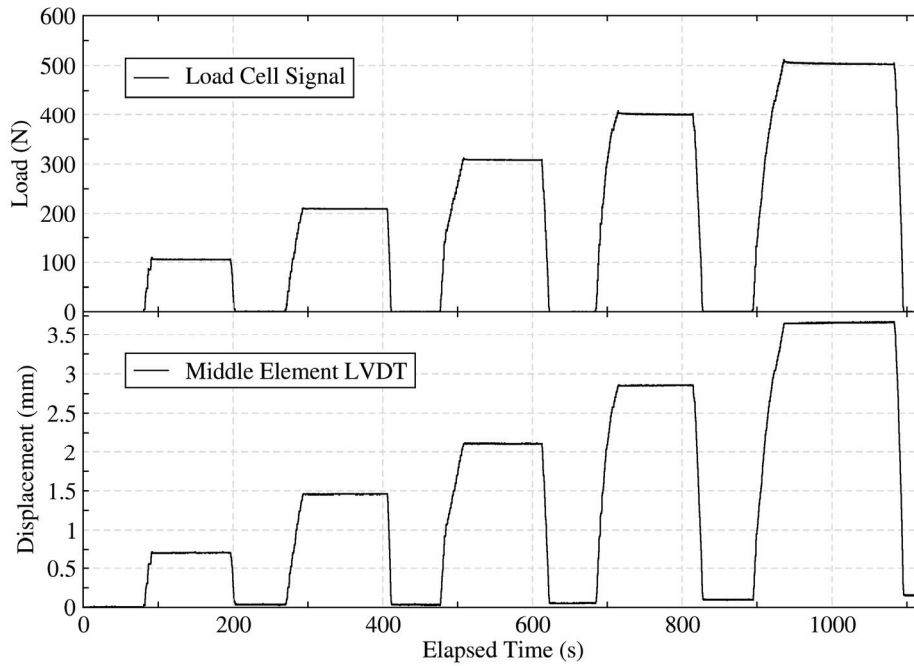


Figure 15: Time Series Plot of Solid Rod Test

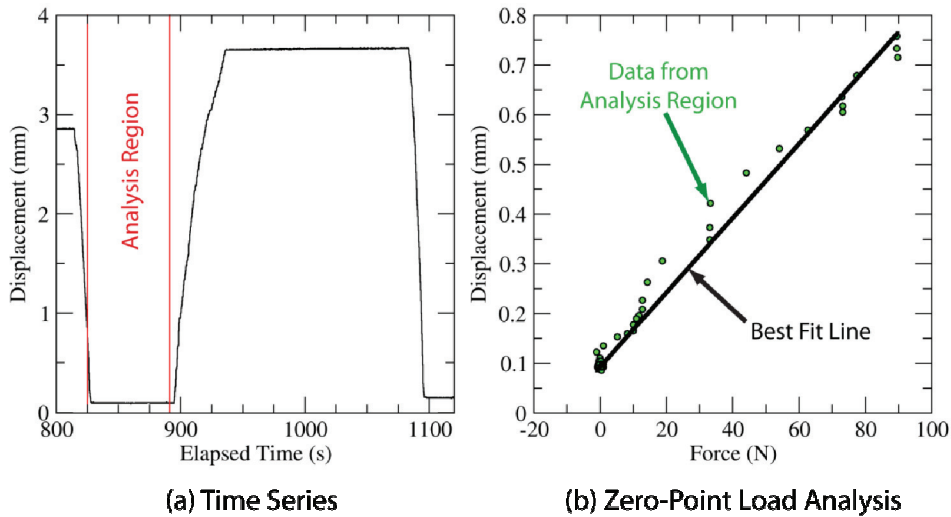


Figure 16: Analysis of LVDT Displacement Prior to Load Cycle

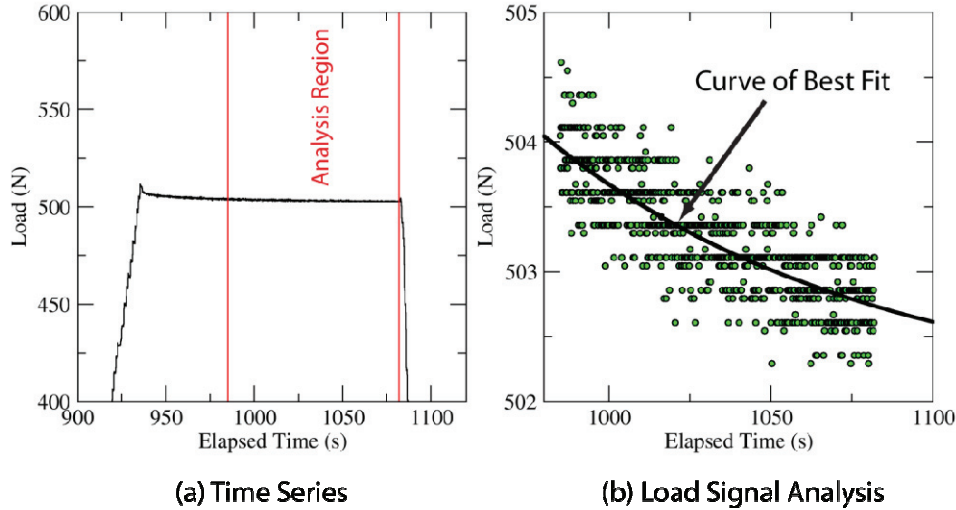


Figure 17: Analysis of Load Cell Signal at Maximum Displacement of Load Cycle

The load cell signals decay with time when the higher loads are applied, as shown in Figure 17(a). This is also seen to a lesser degree with the LVDT signals. To account for this time-dependence and determine the steady-state peak measurement, an exponential function is fit to the data and the value of the function at infinite time is used as the measured peak value. The exponential function does fit the data well, as shown in Figure 17(b), and its extrapolation is a better estimate of the maximum steady-state load than evaluating the average load from the end of the load cycle.

As was performed for the initial full-bundle validation tests, the maximum measured values can be determined from the difference in the peak and initial values and the permanent deformation is determined from the difference in the final and initial values.

Each test response was evaluated to determine the bias of the data. This was evaluated by fitting a straight line to the initial set of load cycles where a linear response and no permanent deformation was observed. The bias on the load for each test was determined from the y-intercept of the fit and removed from the experimental data.

3.3 Verification of Experimental Apparatus

A series of three tests with solid rods in a 3-point test arrangement shown in Figure 12 were performed at Stern Laboratories (Snell, 2009). All five LVDTs were used to measure the displacement of the rod at different locations along its axis. The response at all LVDTs was linear and the best fit was calculated from the 3 test data sets using linear regression. Plots of the measured LVDT responses along with the best fit are given in Figure 18 to Figure 20.

The reproducibility of the three tests was quite good. The displacement reproducibility as measured by the LVDTs located near the center of the rod was excellent with observation showing little noticeable deviation. This was not the case for the LVDTs located near the ends of the elements where the displacement magnitudes were much smaller. These displacements are on the order of the accuracy of the LVDTs and this influenced the scatter of the measured displacements. Other effects due to the location of the supports along the rod might also have had a small effect on the recorded displacements.

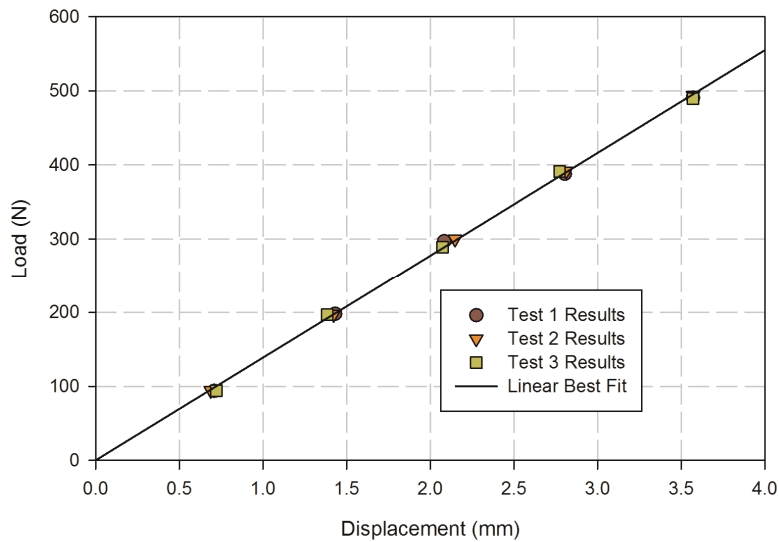


Figure 18: Solid Rod Response Measured at Middle LVDT

A comparison of the experimental results was made with 3-point bending analytical equations and a finite element simulation using ANSYS. In the experiment, the load was applied to the center of the rod using the element pull loading fixture (Figure 13) and the supports were located at different distances from the ends of the rod. This is equivalent to a 3-point bending arrangement with the load applied away from the center of the beam. The geometry and equations used to evaluate the expected deflection of the rod at the LVDT locations is shown in Figure 21.

The ANSYS calculations were performed to simulate the experimental conditions and geometry as best as possible. The solid rod dimensions and material properties were simulated with expected values² and the finite element geometrical model and mesh was chosen to match the real experiment as close as possible. The finite element model is shown in Figure 22 and fixed displacement loads are applied to the rod.

There is uncertainty in modelling the application of the load on the rod. The push fixture is approximately 25 mm long and as the rod deforms, the surface of the rod is not straight like the push fixture. Therefore, contact between the rod and fixture is expected to be at the ends of the fixture. As shown in Figure 22, loads were only applied to the rod near the ends of the fixture, but the FE results tend to be sensitive to the number of axial nodal planes with fixed displacements. As more planes are fixed, extra stiffening is added to the model, which is not physical since the rod is not fixed during the experiment. Therefore, a single axial plane on each end of the fixture was chosen, but this arrangement is not true 3-point loading as can be seen in Figure 23, where the interference in the stress field along the rod is apparent during loading. However, since the two loading points are relatively close together relative to the overall length of the rod, the deformation of the rod can be well represented by 3-point loading.

² Material properties for the SS304 rod material were not well characterized. Stainless Steels have elastic modulus values between 190 GPa to 210 GPa, but 193 GPa was chosen since several manufacturers list this value for SS304.

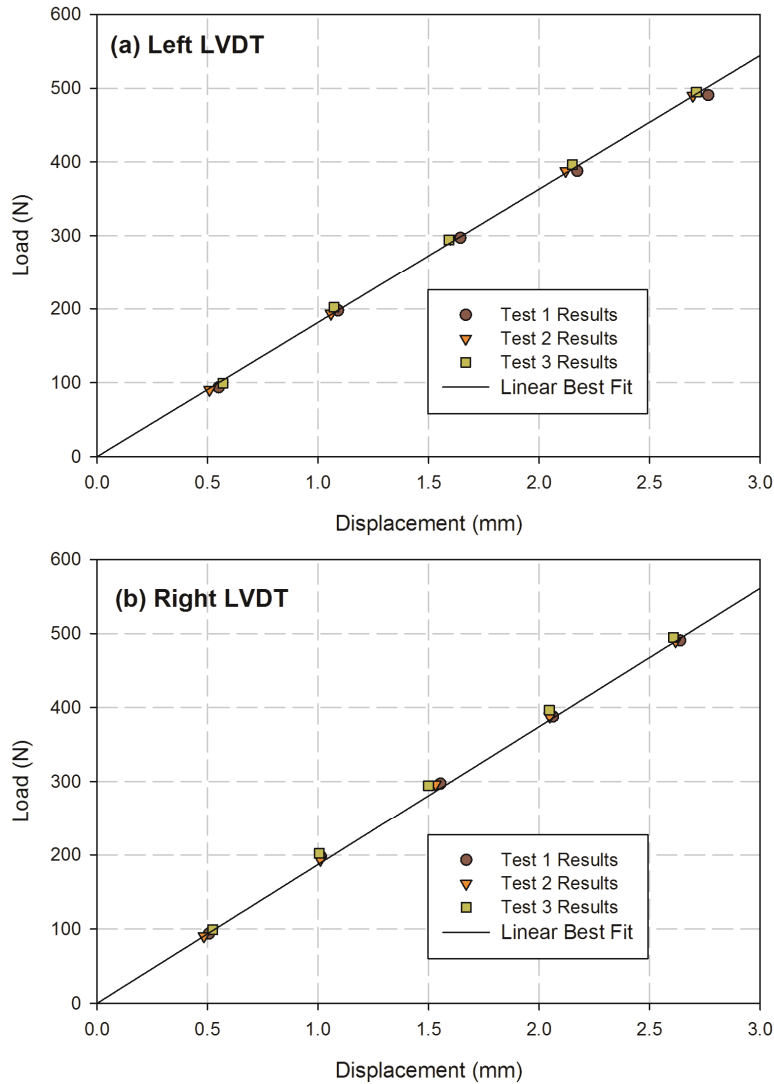


Figure 19: Solid Rod Response Measured at Inner LVDTs

A comparison of the experimental best fit lines with the analytic expression for 3-point bending and the ANSYS simulations are given for each LVDT in Figure 24 to Figure 26. The stiffness results (taken as the slope of the response) are also given in Table 2. The agreement between the three sets of data for the middle and inner LVDTs is reasonably good. The ANSYS response is stiffer than the theoretical response by approximately 1%. This is expected because of the additional stiffening the pull load fixture will add to the rod.

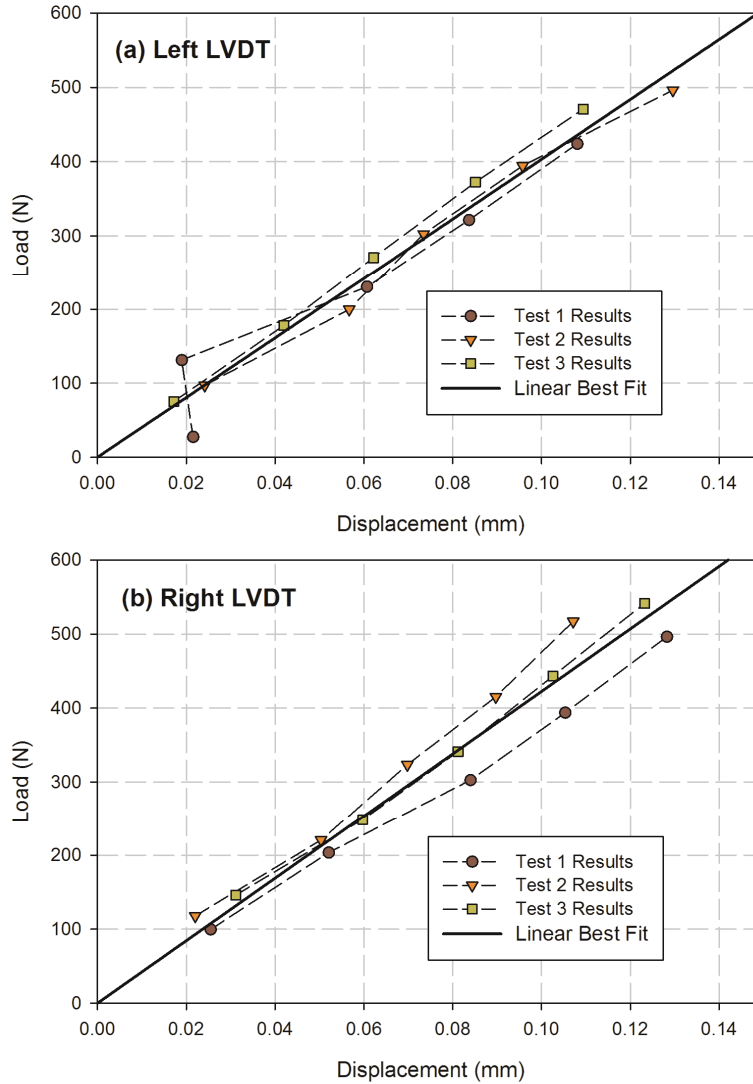


Figure 20: Solid Rod Response Measured at Outer LVDTs

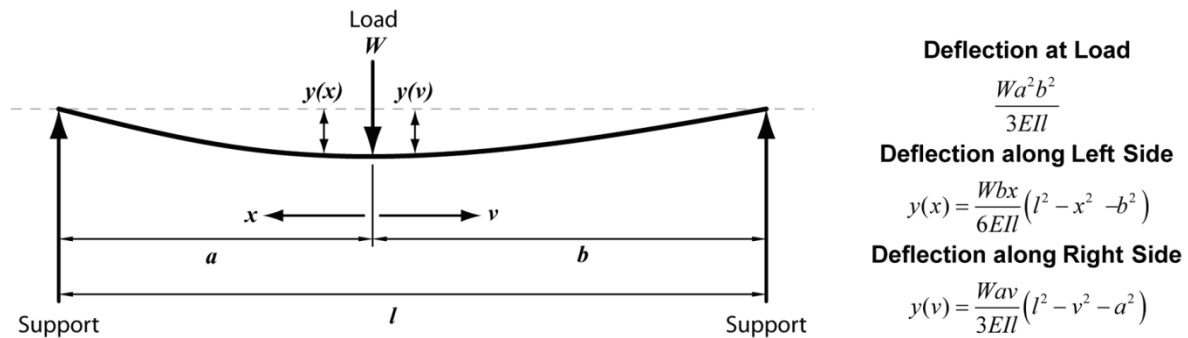


Figure 21: Analytic Equations used for Off-Center 3-Point Bending

The experimental response for the middle and inner LVDTs is about 4-6% less stiff than the theoretical response and about 5-7% less stiff than the ANSYS response. With the experimental uncertainty determined from the three test datasets the experimental response does not agree with the 3-point bending response. The increase in the flexibility of the rod in the experiments is surprising since one would expect the rod to be slightly stiffer than the 3-point response because of the pull load fixture clamp. One possible explanation for this is the elastic modulus of the manufactured rods is slightly less than the standard specification for SS304. A modulus of approximately 187 GPa appears to provide better agreement between the theoretical and experimental responses.

Table 2: Solid Rod Verification Analysis Results

LVDT (distance from support)	3-Point Bending (N/mm)	ANSYS Model (N/mm)	Experimental (N/mm)
Outer Left (5 mm)	4,189	4,762	4,031
Inner Left (125 mm)	188	191	182
Middle	144	146	139
Inner Right (115 mm)	199	200	187
Outer Right (6 mm)	3,459	4,503	4,224

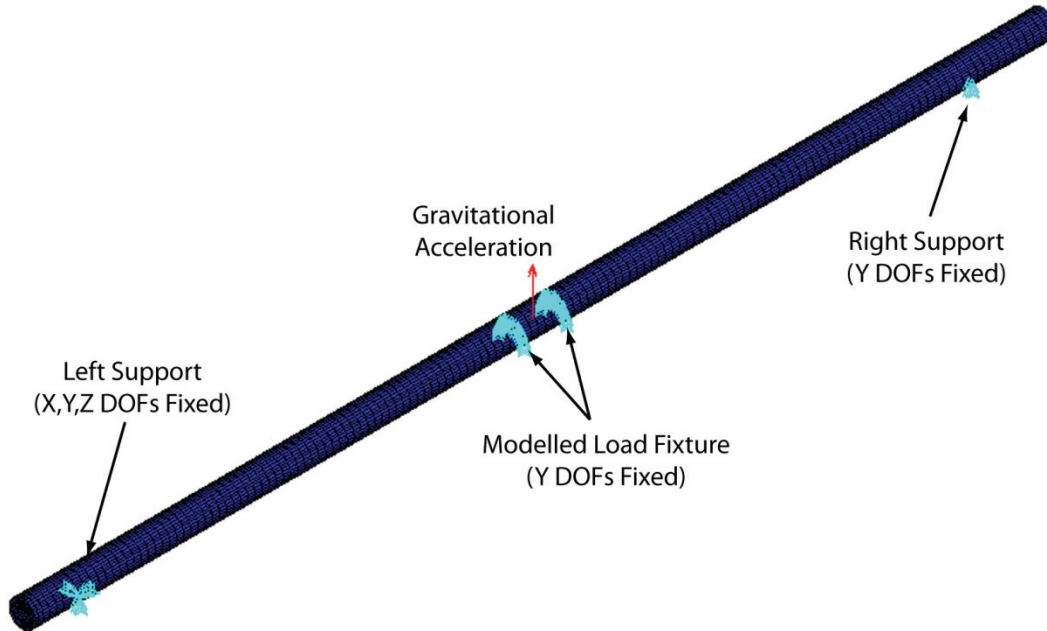


Figure 22: ANSYS Finite Element Model used for Solid Rod Validation Test Modelling

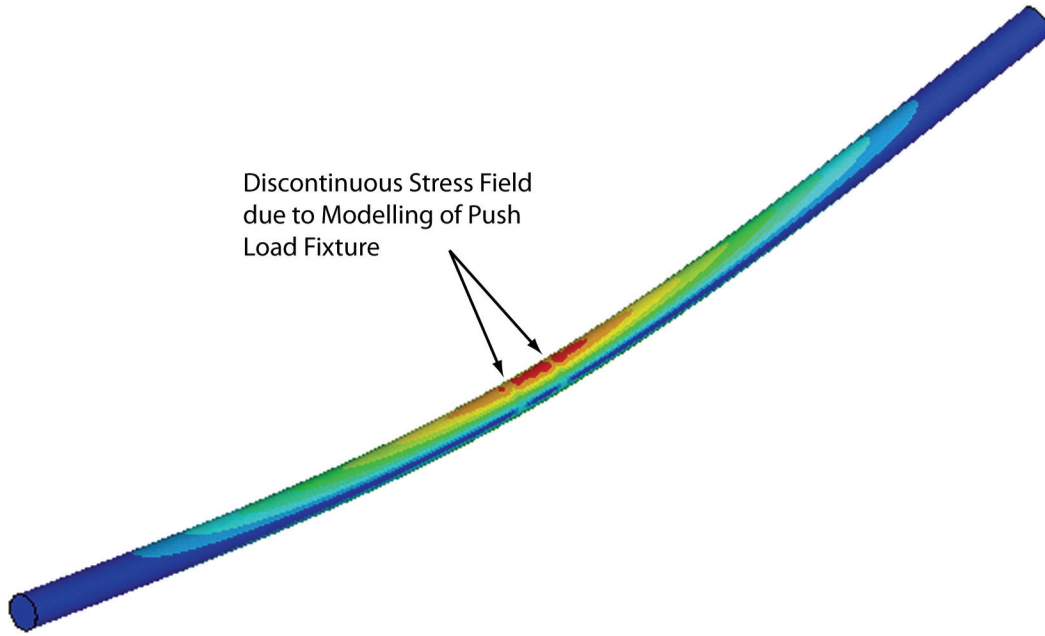


Figure 23: Solid Rod Finite Element Model von Mises Stress Field under Loading

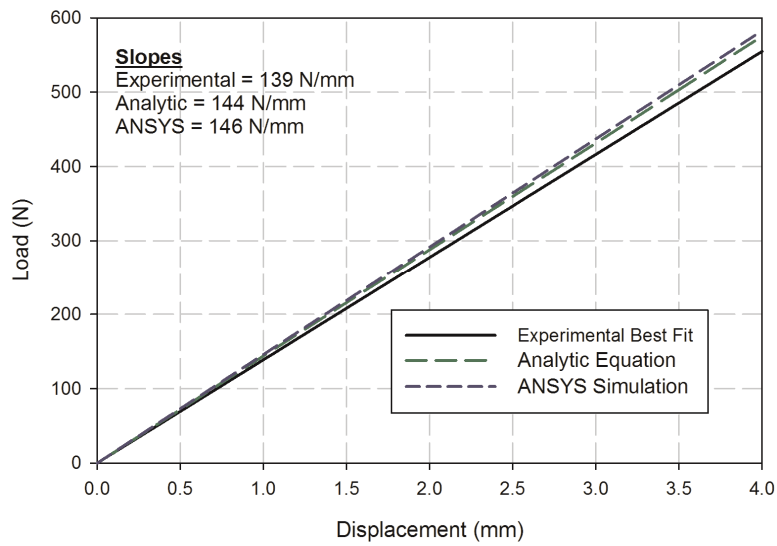


Figure 24: Solid Rod Experimental and Calculated Middle LVDT Responses

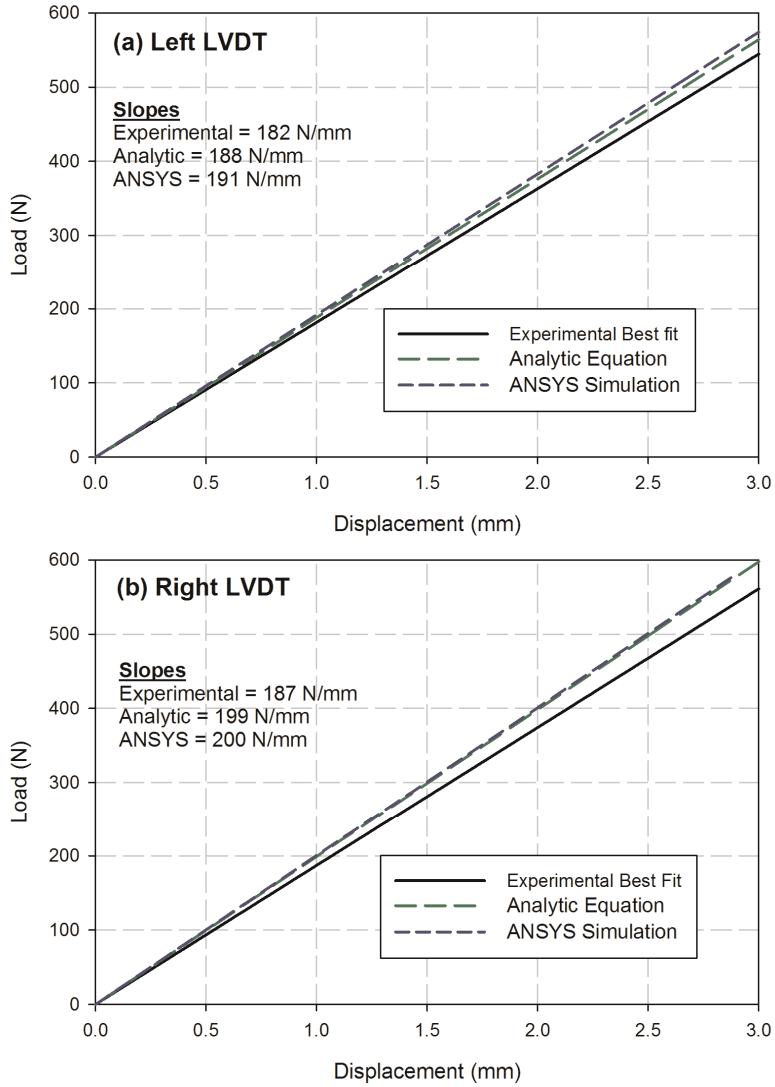


Figure 25: Solid Rod Experimental and Calculated Inner LVDT Responses

The response of the outer LVDTs does not show the same level of consistency between all three stiffness responses. However, this is expected to be a result of the LVDT locations being very close to the supports. The experimental response was on the order of the LVDT uncertainty and local effects at the supports in the finite element calculation influence the comparison of responses. Because of this, the outer LVDT results for the solid rod tests are not considered in this analysis.

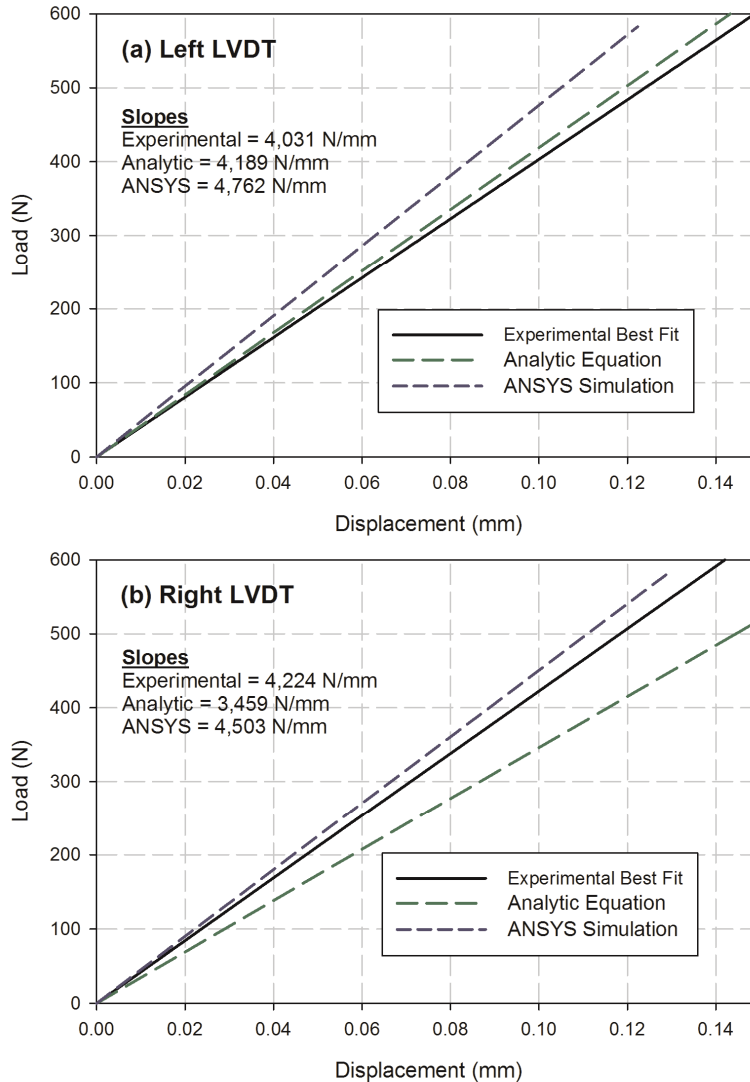


Figure 26: Solid Rod Experimental and Calculated Outer LVDT Responses

3.4 Single Element Validation Results

A series of eight tests were performed on 28- and 37-element fuel elements. A 3-test series involving multiple load cycles similar to the validation tests was performed for each fuel element design. Additionally, two tests with one and two load cycles, respectively, were performed for the 37-element fuel design to evaluate any effects multiple that load cycles might have on the fuel element response. The results of these tests are presented here.

3.4.1 28-Element Fuel Elements

The LVDT displacement results for the three 28-element tests are shown in Figure 27 to Figure 29. Unlike the solid rod tests, the middle LVDT is equidistant from the fuel element supports. The best linear fit through the origin to the experimental data was obtained and plotted. The fit is not based on the whole dataset because the response is not linear for all loads. Instead, the fit is based on the lower load data that displays a linear response.

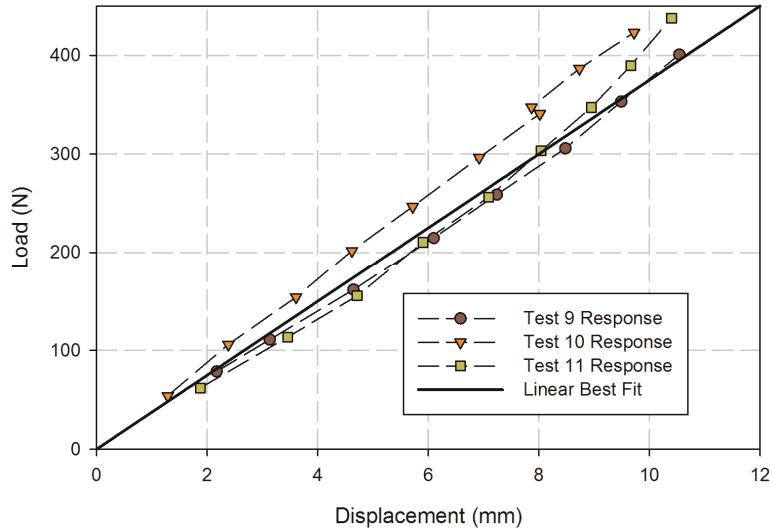


Figure 27: 28-Element Response Measured at Middle LVDT

The unusual response seen in the inner LVDTs at the higher displacements is a result of over-ranging the LVDTs. The range of the LVDTs used in this location is approximately 6 mm.

The single element tests showed a much stiffer element than seen in the full-bundle tests. This can be seen in Figure 30. The source of this additional stiffness is not currently understood. However, at low deformation/forces, less than 5 mm or 150 N, both sets of experimental data show consistent results.

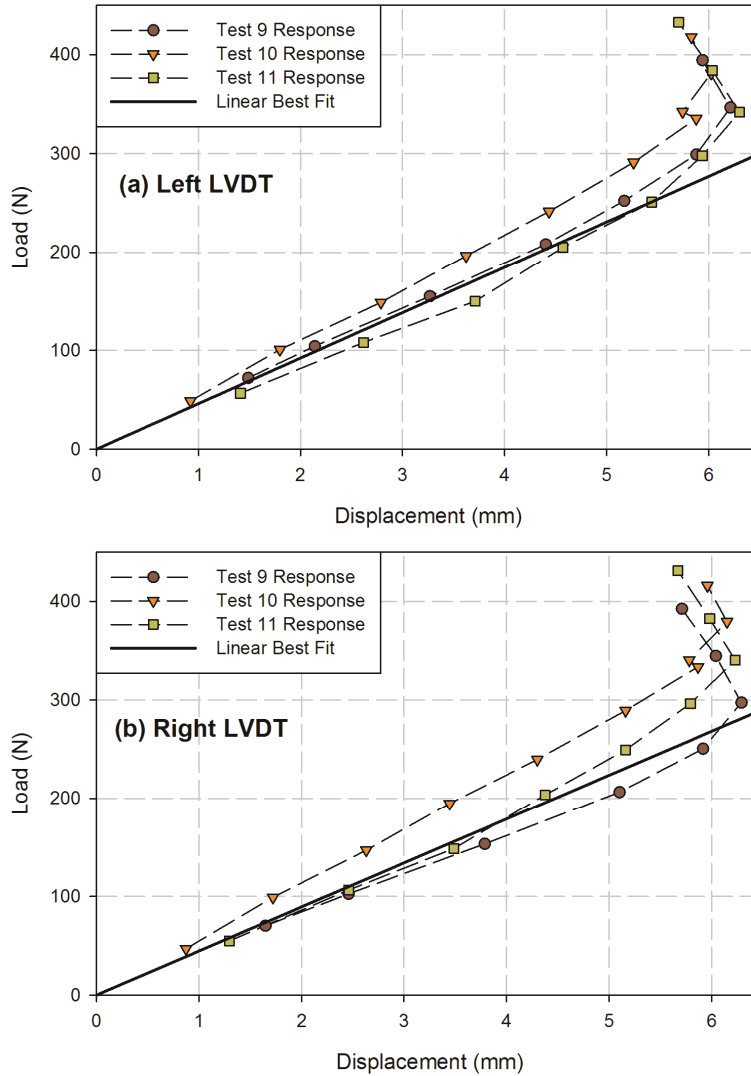


Figure 28: 28-Element Response Measured at Inner LVDTs

3.4.2 37-Element Fuel Elements

The LVDT displacement results for the three tests are shown in Figure 31 to Figure 33 for the 37-element design fuel elements. The response that was measured for the single fuel elements is very similar to the response seen in the full-bundle pull tests. Figure 34 is a graph of the full-bundle and single element experimental results. Both sets show the same stiffening response and are nearly identical given the scatter in the data.

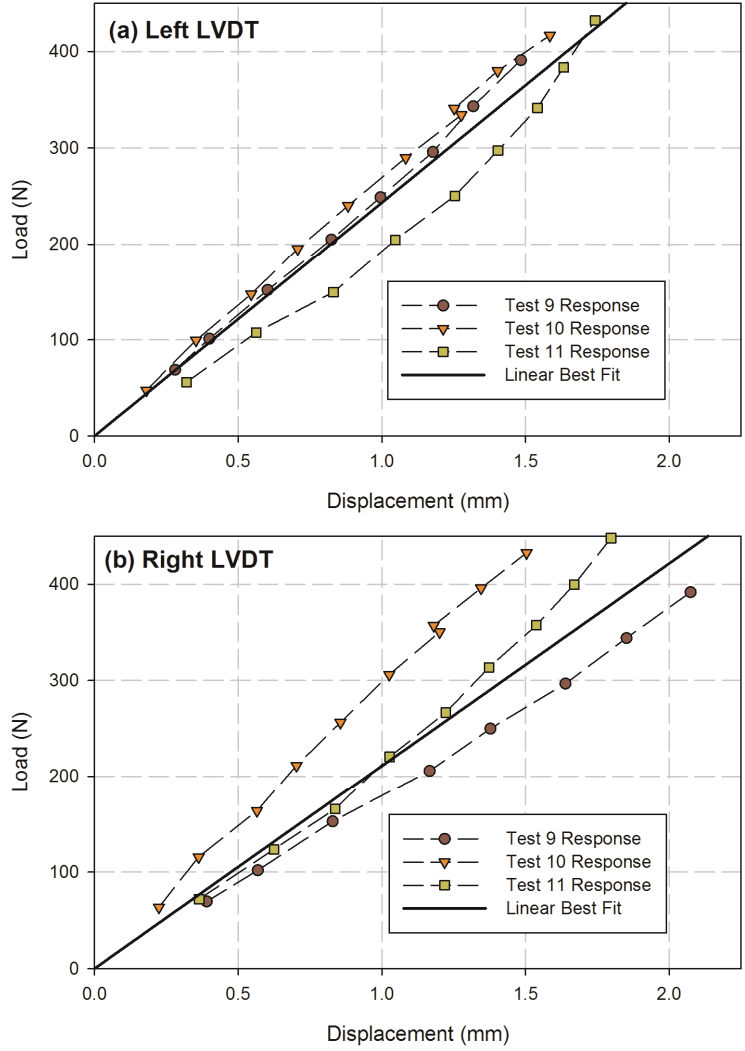


Figure 29: 28-Element Response Measure at Outer LVDTs

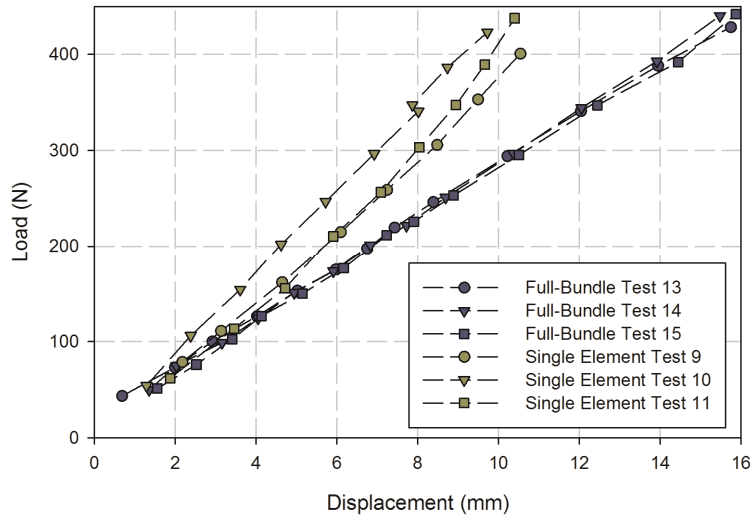


Figure 30: Comparison of 28-Element Full-Bundle and Single-Element Test Results

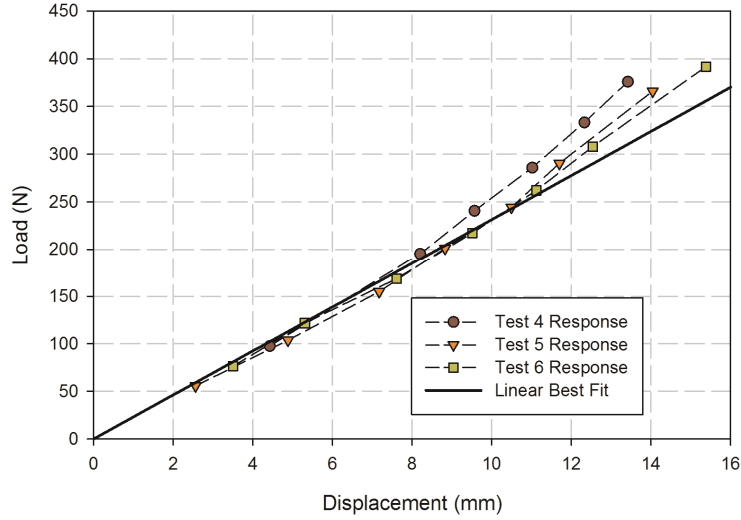


Figure 31: 37-Element Response Measured at Middle LVDT

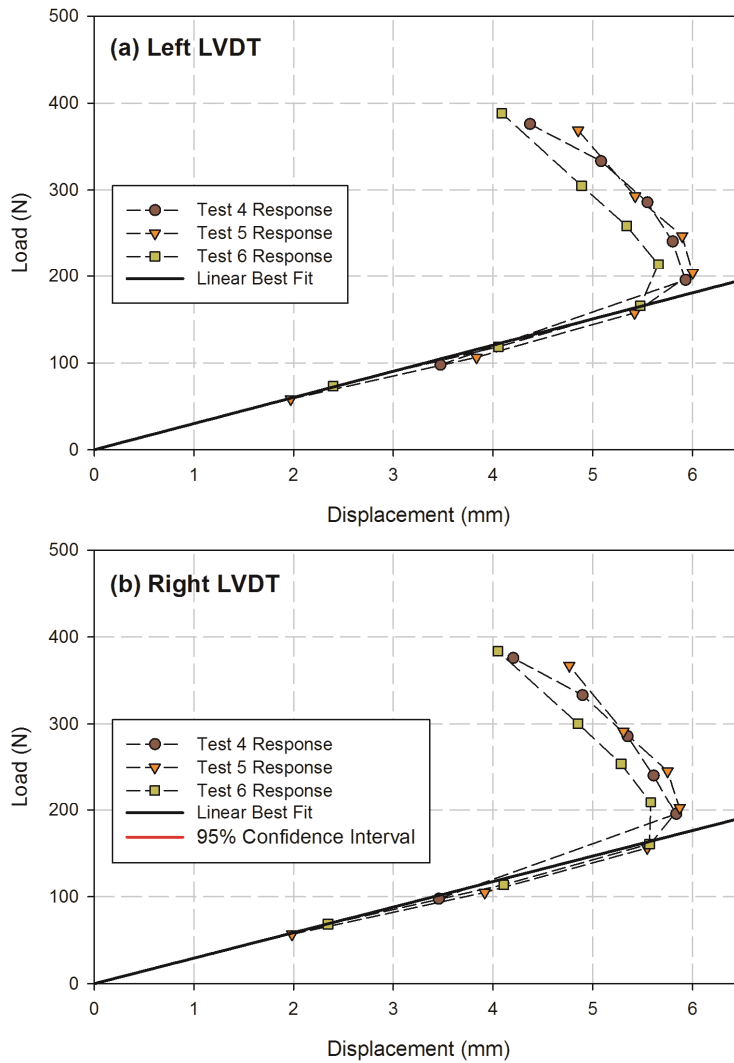


Figure 32: 37-Element Response Measured at Inner LVDTs

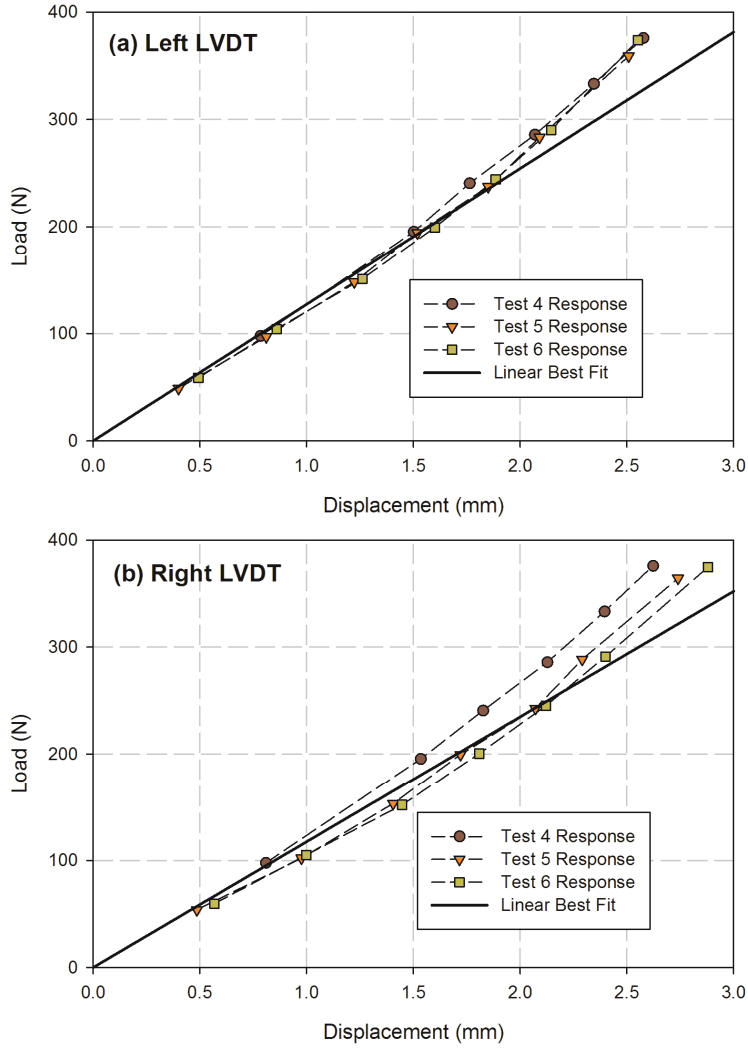


Figure 33: 37-Element Response Measured at Outer LVDTs

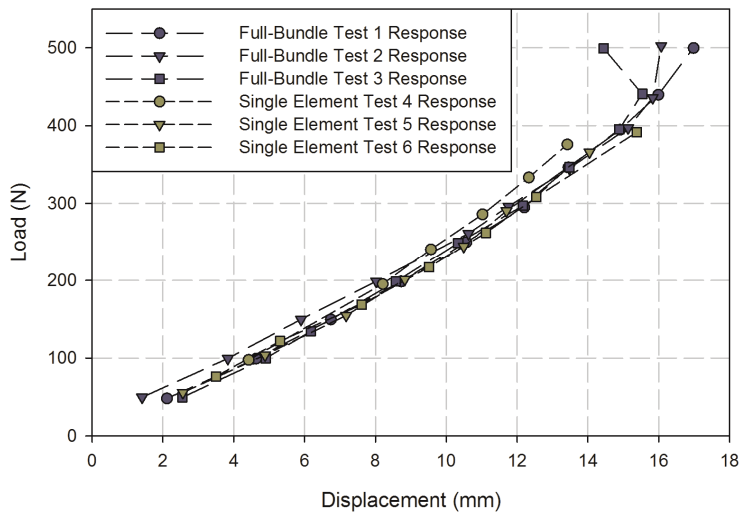


Figure 34: Comparison of 37-Element Full-Bundle and Single-Element Test Results

4. FUEL ELEMENT MODEL VALIDATION

The following sections present the validation of the 28- and 37-element interaction finite element models against the single-element validation experiments performed at Stern Laboratories. Validation of the pipe finite element model was not performed as it does not account for the pellet effects.

4.1 Validation of 28-Element Model against Single Element Tests

The new fuel element model described in Section 2.2 was validated against the recent mechanical tests performed at Stern Laboratories. The fuel bundle model was prepared to simulate these tests by disabling creation of all fuel elements except one from the outer ring. Large regions of the endplate, which are not used in this simulation, were also deleted from the model for this purpose.

The test conditions were simulated in detail. The non-axial loads were simulated by applying fixed displacements on the middle bearing pad surface nodes. The regions of the endplate that were clamped by the test apparatus were modelled by suppressing node movements in all directions. The schematic of the mechanical test is presented in Figure 35.

The material properties and the design parameters of the 28-element bundle model were set to their nominal values, as indicated in the fuel design description (Køhn *et al.*, 2002). A nominal value for the sheath thickness is not provided in the fuel design description and a value of 0.45 mm was selected, which is within the design tolerance range of 0.38 mm to 0.47 mm to give the best fit to the experimental data at low displacement. In the low forces and displacement region of the element response, where the pellet-to-pellet and pellet-to-sheath interactions are playing a secondary role, the sheath thickness is one of the key parameters that will influence the fuel element mechanical behaviour.

The value of the axial gap has not been well characterized and is not supplied in the fuel design description. For this analysis, the axial gap between pellets has been set to 0.02 mm. This selection of the pellet-to-pellet gap is supported by the sensitivity study presented in the next section, where a wide range of axial gaps from pellets initially in contact, to pellets that are not interacting axially have been evaluated.

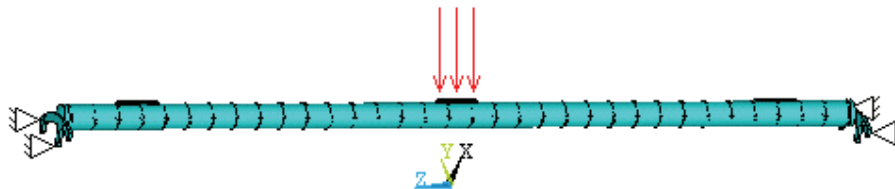


Figure 35: Non-Axial Load Test Simulation Boundary Conditions and Geometry

The displacements applied to the fuel element center bearing pad were 2, 4, 6, 8, 10, 12, and 12.5 mm. These applied displacements correspond to the displacement measured on the

middle LVDT. For each simulated load, the reaction forces in the nodes having imposed displacements were cumulated to obtain the total reaction force, which represents the load measured on the load cell during the experiment. Calculated and measured force and displacement responses at the element center (see Figure 27 for experimental data analysis) of the 28-element fuel element are presented in Figure 36. The agreement between 28-element fuel element model predictions and the measurements is very good. The effect of fuel element stiffening at high loads is correctly predicted by the fuel element model with interface elements between the pellets and the sheath.

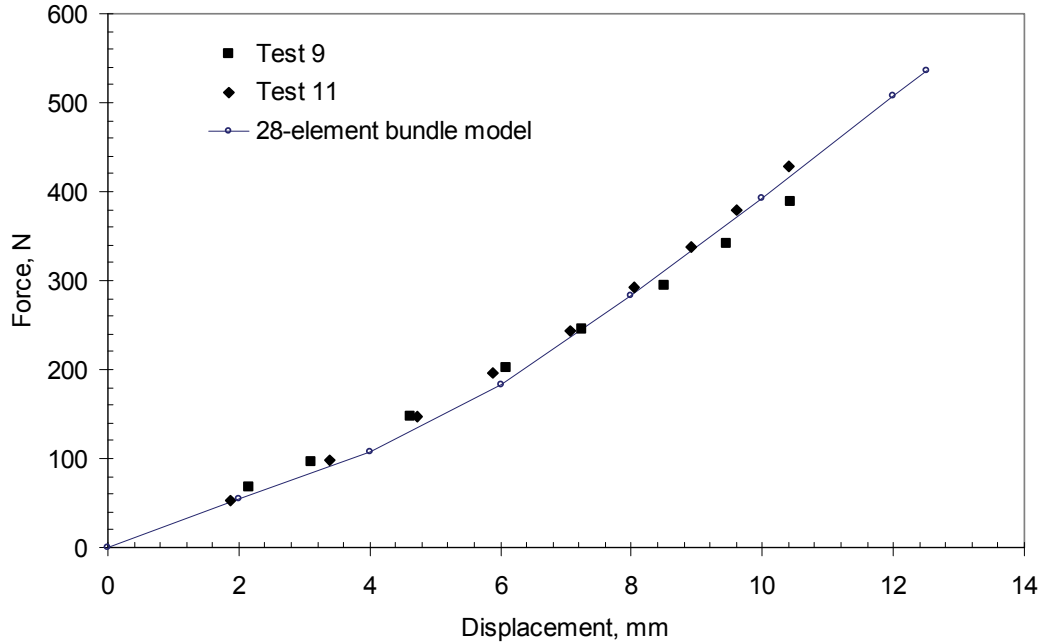


Figure 36: Measured and Modelled Response of 28-Element Fuel Element

In addition to the direct comparison between the experimental data and bundle model predictions, the deformation of the fuel element was studied using two bounding analytical cases. Both analytical solutions are for a beam with annular cross section having the elastic modulus, length, diameter, and wall thickness equal to the fuel element sheath. The pellets and the pellet-to-sheath interaction are neglected.

The first analytical case is a beam having both ends clamped, as depicted in Figure 37(a). The maximum deflection of the beam (y) is (Pilkey, 1994):

$$y = \frac{2F}{3EI} \frac{a^3 b^2}{(3a+b)^2} \quad (1)$$

where F is the applied force, E is Young's modulus, I is the moment of inertia, and a & b are the distances between the beam ends and the force application point. The moment of inertia for an annular cross-section is:

$$I = 1/4 \pi (r_0^4 - r_i^4) \quad (2)$$

with r_o and r_i being the outer and inner radii of the sheath.

The second analytical case is for the deflection of a simply supported beam. In this case, the maximum deflection of the beam is given by Pilkey (Pilkey, 1994):

$$y = \frac{F a}{6LEI} \left[-(L-x)^3 + (L^2 - a^2)(L-x) \right] \quad (3)$$

where x is the longitudinal location where the deflection is evaluated, in this case $x = L/2$, (the equation is valid for $x \geq a$) and L is the length of the beam, which equals $a + b$. This case is presented in Figure 37(b).

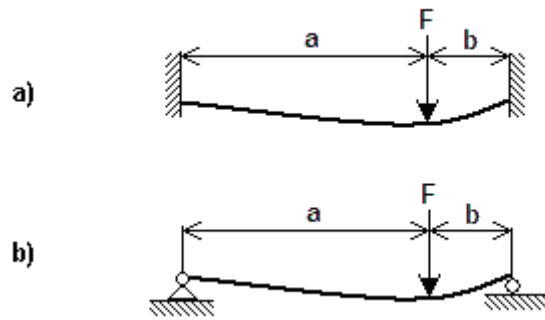


Figure 37: Analytical Cases Describing (a) Fixed Beam and (b) Simply Supported Beam

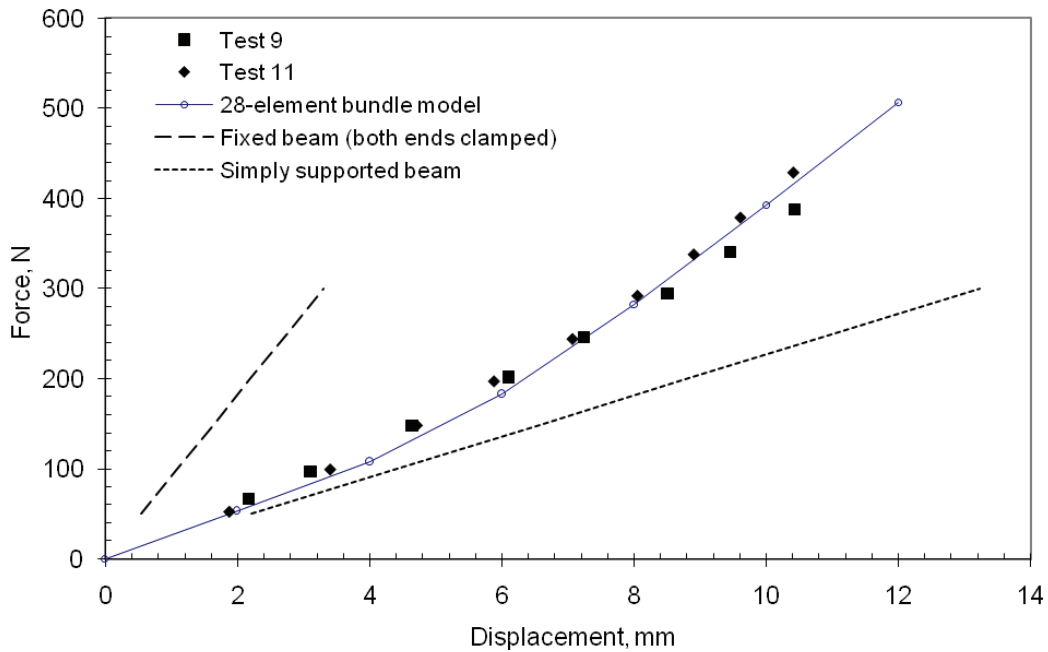


Figure 38: Comparison of Responses of the 28-Element Fuel Element

The predictions obtained with the analytical solutions are presented in Figure 38. The deflection predicted for the case of a partially fixed beam (dotted line) is in agreement with the experimental measurements and bundle model predictions for low loads where the sheath dominates the response. At high loads, due to the stiffening effect, the mechanical response of the fuel element diverges from the analytical solution. In most of the practical applications for which the radial gap is closed, the mechanical response of the fuel element is expected to change towards the case of the simple beam clamped at both ends (dashed line).

During the deformation of the fuel elements the maximum equivalent (Von Mises) stress was obtained in the endplate in the vicinity of the endplate-endcap weld. For a 2 mm deformation at the centre of the fuel element the maximum equivalent stress in the endplate predicted by the 28-element bundle model was 215 MPa, as shown in Figure 39. In comparison, for the 12.5 mm deformation case, the equivalent stress increased to 1,296 MPa, as shown in Figure 40. At such high values of the stress the endplate is deformed in the plastic regime and can account for the permanent deformation observed at high loads in the experiments.

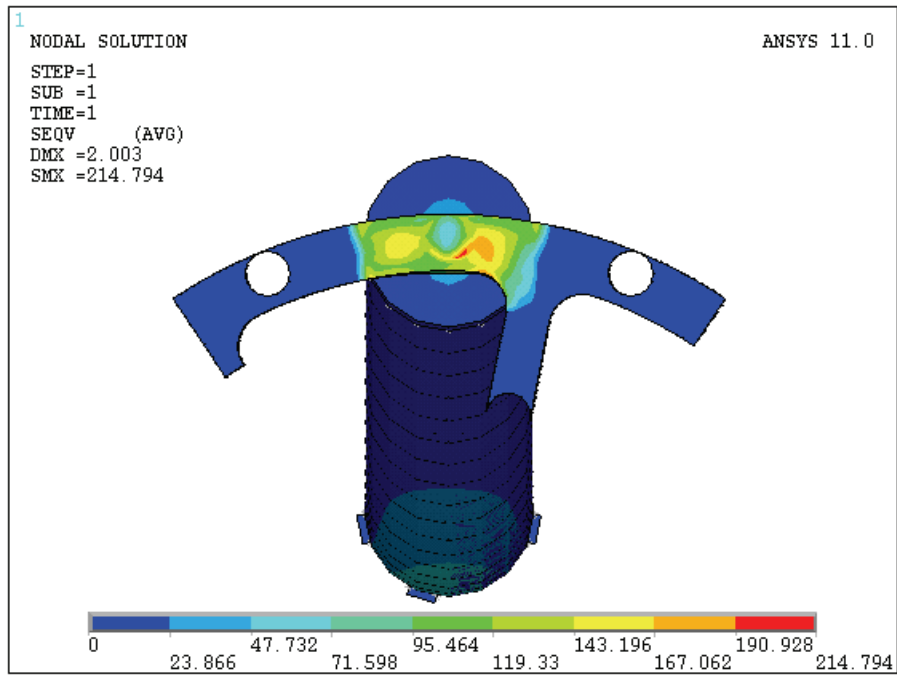


Figure 39: Equivalent Stress in the 28-Element Endplate for 2 mm Deformation³

³ The deformation of the fuel element is plotted on an exaggerated scale for the modelling results.

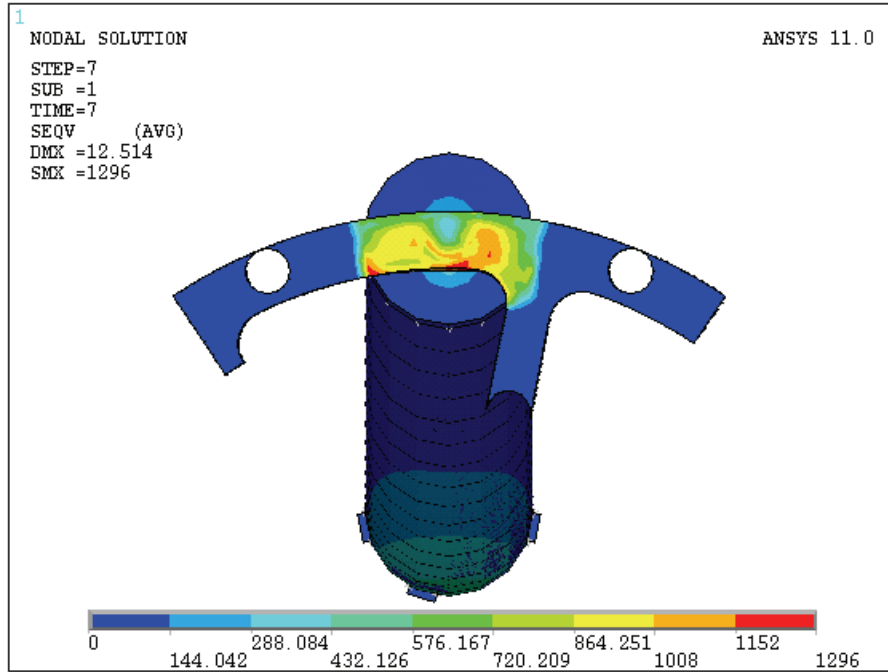


Figure 40: Equivalent Stress in the 28-Element Endplate for 12.5 mm Deformation

In Figure 41 the calculated equivalent strain predicted for an applied displacement of 12.5 mm is presented in a vertical section of the fuel element that passes through the centreline.

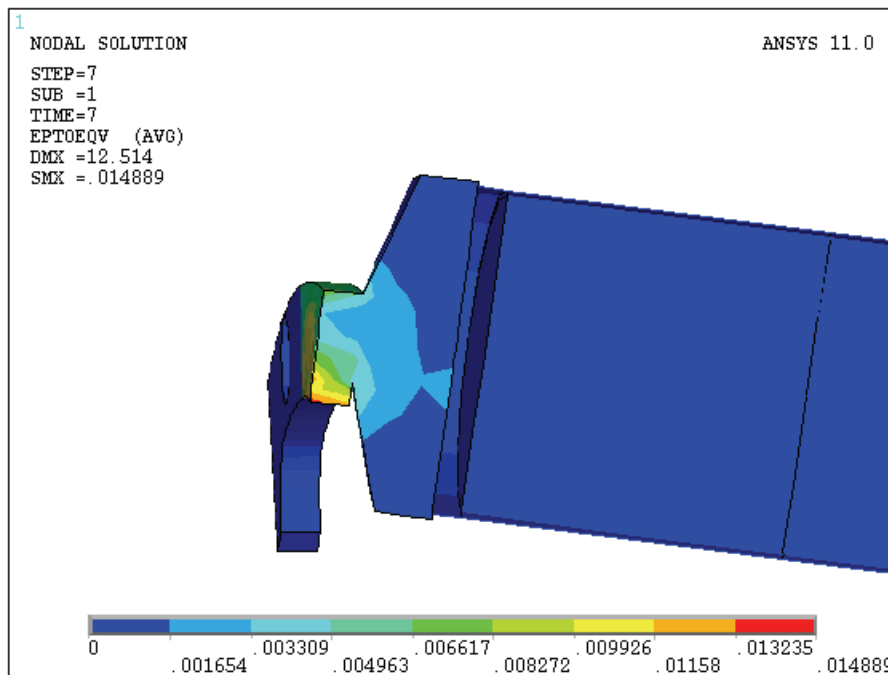


Figure 41: Equivalent Strain in the 28-Element Endplate for 12.5 mm Deformation

Lower values of the equivalent stress and equivalent strain were predicted for the sheath of the fuel element in comparison with the endplate. For the case where a deformation of 12.5 mm was applied, the stress in the sheath was still in the elastic domain, see Figure 42.

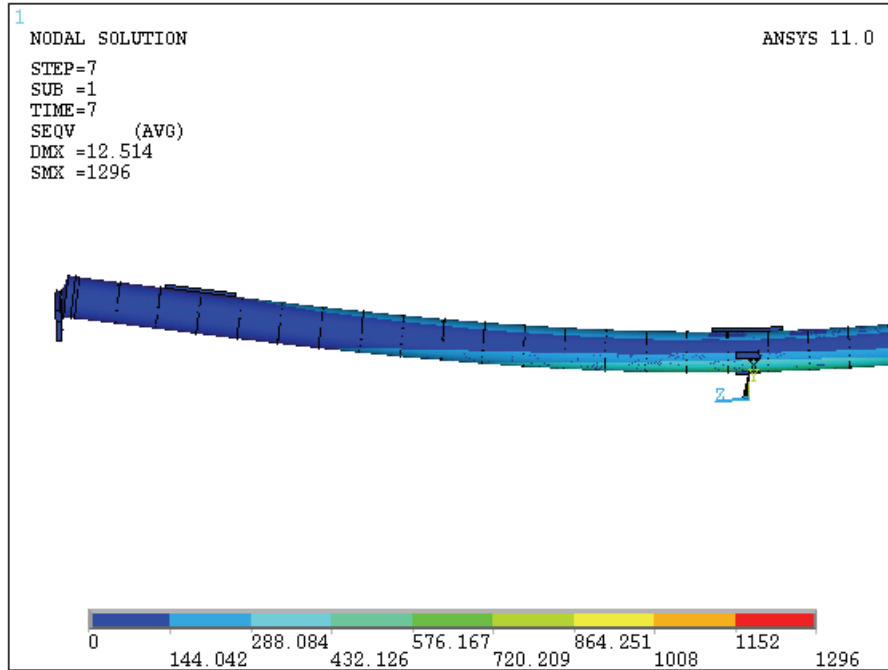


Figure 42: Equivalent Stress in 28-Element Sheath for 12.5 mm Deformation

At higher mechanical deformations, for example near the displacement of 12.5 mm at the middle of the fuel element, the radial gap is closed for approximately 10–12 pellets located at the middle of the fuel element. Figure 43 presents the interior surface of the interface finite elements obtained by sectioning the elements with a vertical plane that passes through the fuel element axis of symmetry. The highest interface closure was around -0.04 mm (negative values denote closure) and equals the nominal radial gap modelled in this simulation. Similar behaviour can be noted for fuel deformations of 12, 10, and 8 mm respectively. The 8 mm loading case is presented in Figure 44 and shows that the radial gap is completely consumed for approximately 5 pellets located in the central part of the fuel element. As well, the highest interface closure is consistent with the nominal radial gap of -0.04 mm. For a fuel deformation of 6 mm, the finite element model predicts that the radial gap was not completely closed, as shown in Figure 45.

The average contact pressure between the pellets and the sheath for the entire fuel element is presented as a function of fuel element deformation in Figure 46. The interface pressure presents low values for deformations of 2, 4, and 6 mm respectively. At 8 mm, and at higher deformations, the increased contact pressure indicates a strong pellet-to-sheath interaction.

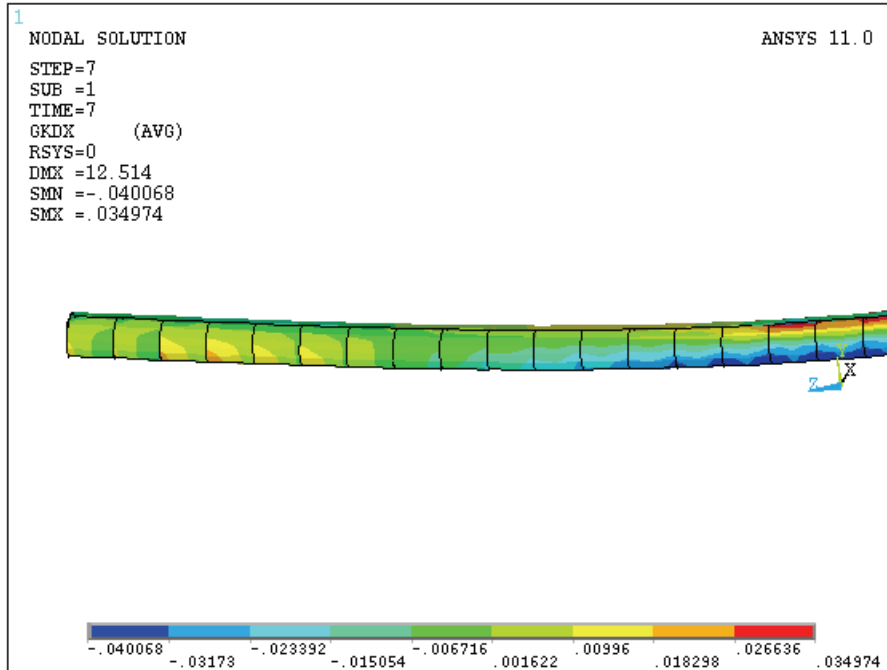


Figure 43: Pellet-to-Sheath Interface Closure for 28-Element Model with 12.5 mm Deformation

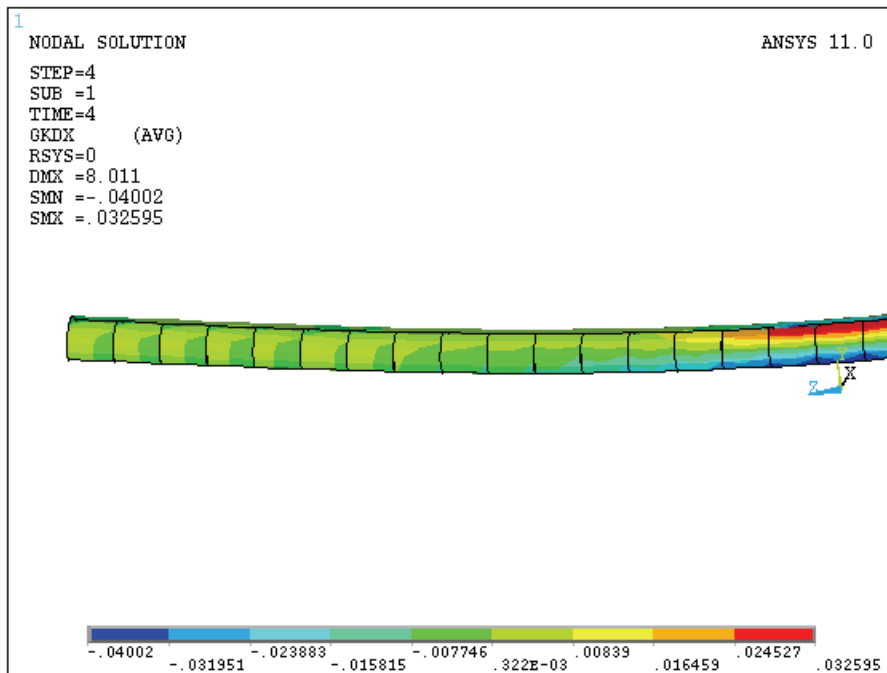


Figure 44: Pellet-to-Sheath Interface Closure for 28-Element Model with 8 mm Deformation

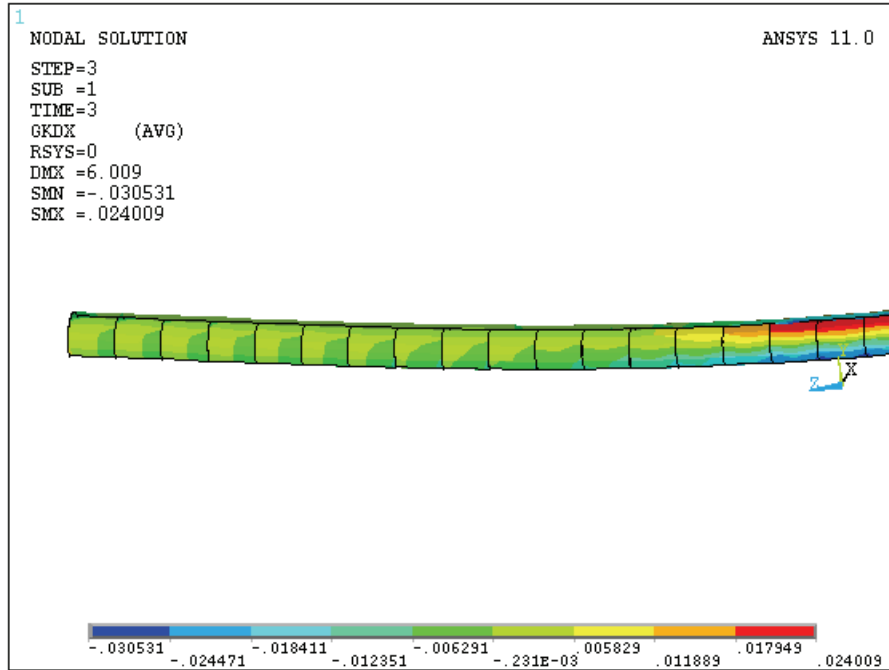


Figure 45: Pellet-to-Sheath Interface Closure for 28-Element Model with 6 mm Deformation

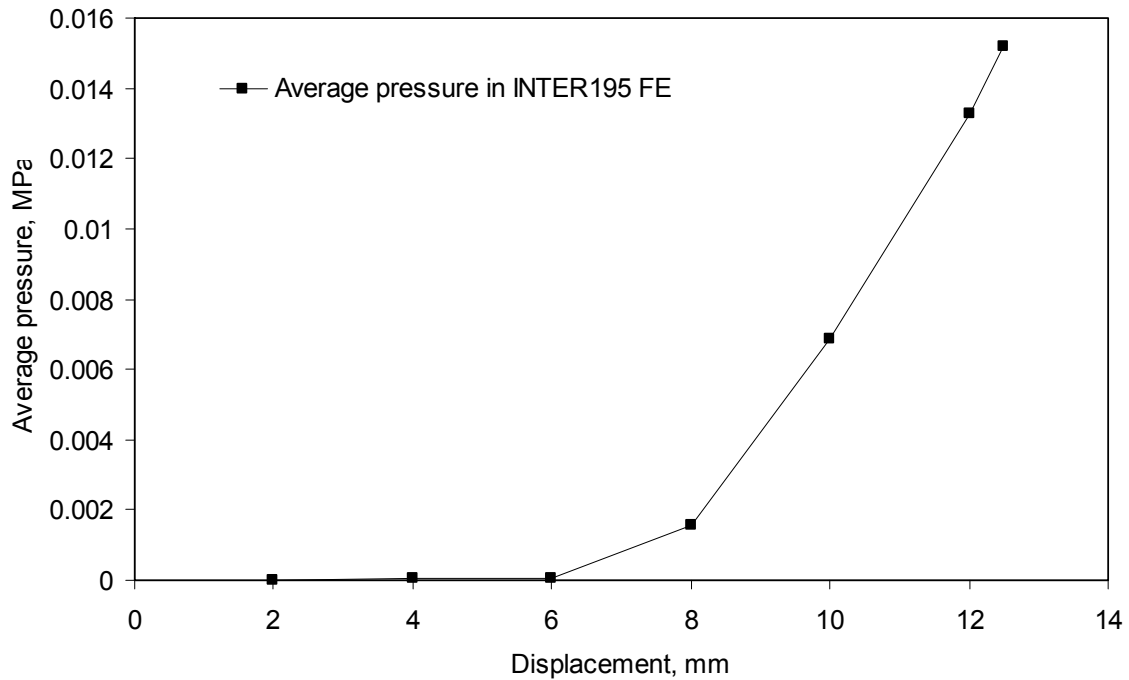


Figure 46: Average Pellet-to-Sheath Pressure vs. 28-Element Deformation

Once the radial gap is closed, the pellets contribute to the fuel element's overall stiffness. The Von Mises stress predicted in the pellets for the case of 8 mm deformation is presented in an axial section through the fuel in Figure 47. The stress values exceeded 100 MPa. For the 4 mm deformation case, the equivalent stress in the pellets is lower than 4 MPa (Figure 48). For the case of 8 mm deformation, the location of the high stresses indicates a strong pellet-to-pellet interaction. The contact pressure between adjacent pellets for 8 mm deformation reached values of approximately 160 MPa. The pressure predicted for the contact finite elements of the pellet-to-pellet interfaces is presented in Figure 49. For the 12.5 mm deformation case, the pellets from a central region of the fuel element are presented in Figure 50 (displacements were scaled by a factor of 10). This pellet-to-pellet interaction is consistent with the fuel element bending.

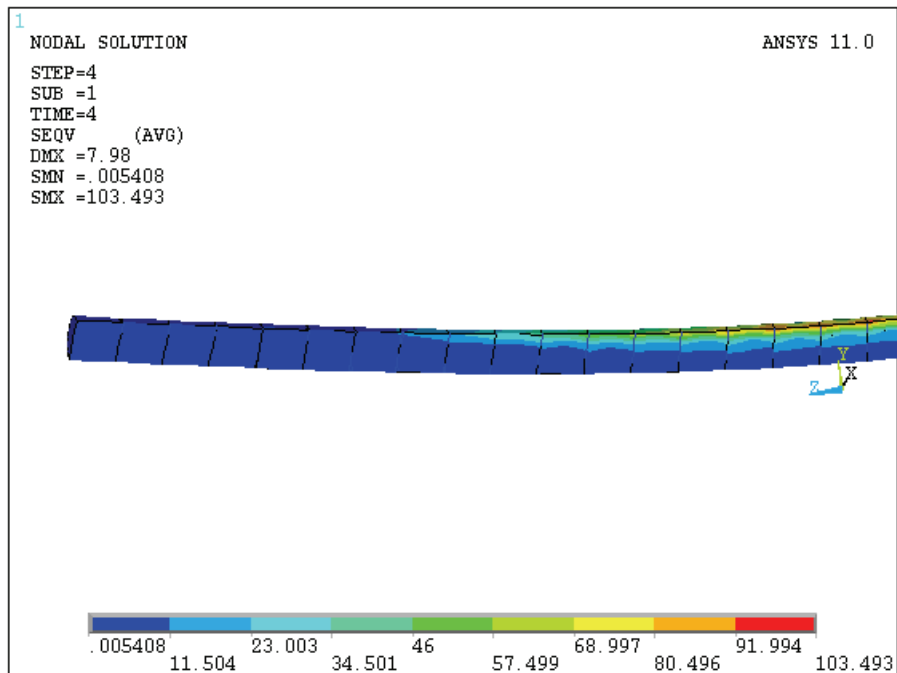


Figure 47: Equivalent Stress in Pellets for 28-Element Model with 8 mm Deformation

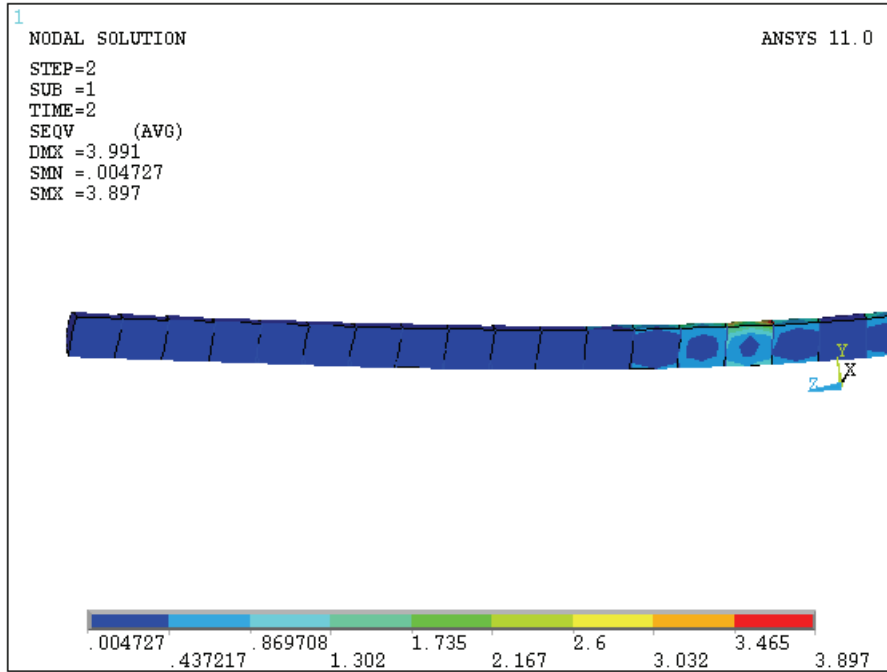


Figure 48: Equivalent Stress in Pellets for 28-Element Model with 4 mm Deformation

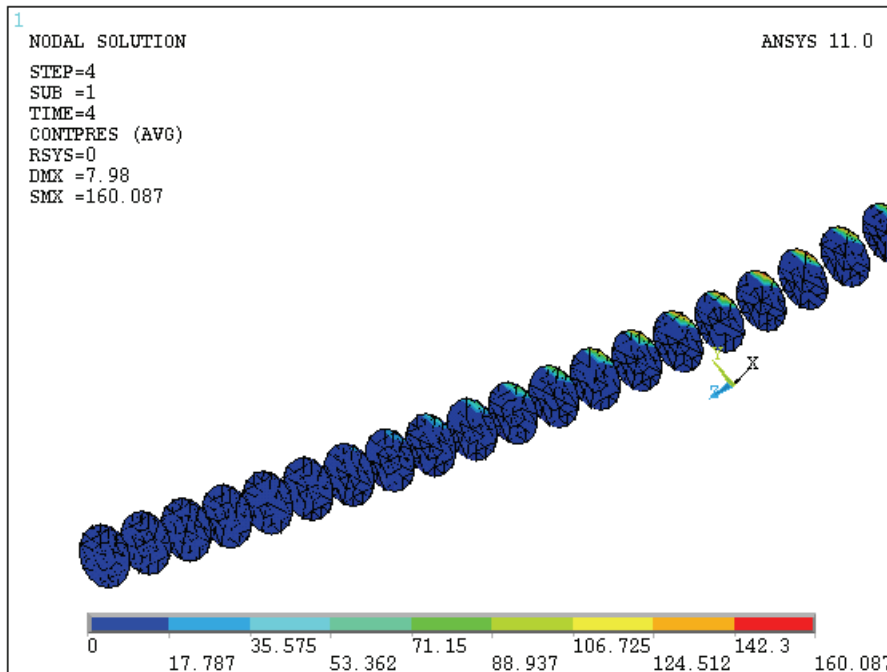


Figure 49: Pellet-to-Pellet Contact Pressure for 28-Element Model with 8 mm Deformation

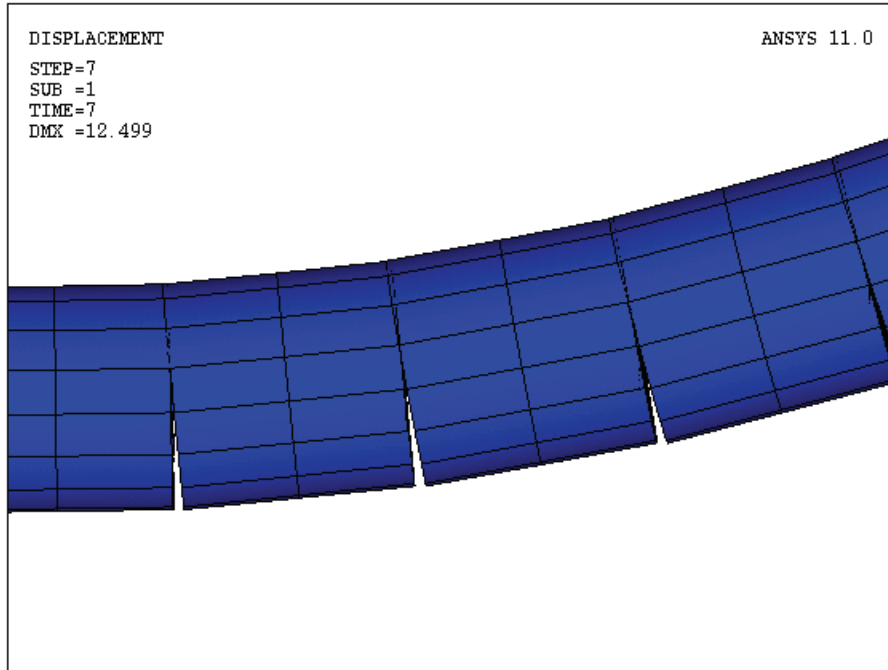


Figure 50: Pellet Interaction of 28-Element Model for 12.5 mm Deformation (10x Scale)

The results obtained for the 28-element fuel element model are in good agreement with the measurements performed on fuel elements subjected to non-axial loads at Stern Laboratories (Snell, 2009). The predicted stresses and strains and the interaction between pellets and sheath or between pellets appear to be consistent with the expected behaviour and range of values. Taking into account the complexity of the mechanical problem, the model can be considered to be very efficient since, for each simulated load step, the solution was obtained in less than 10 iterations.

Some of the parameters used in the model will have to be exercised in a set of sensitivity studies to evaluate their importance over the model predictions and to substantiate the values used for the current study.

4.2 Validation of 37-Element Model against Single Element Tests

Five transversal load tests were performed for 37-element fuel elements at Stern Laboratories (Snell, 2009). In these tests, the outer fuel elements from two different bundles were separated by cutting the endplates. At both ends, small regions of the endplate remain attached to the tested fuel elements and were clamped in the testing apparatus. The non-axial load was applied perpendicular on the fuel element centreline on the middle bearing pad. The schematic of the mechanical test is similar with the tests performed for 28-element fuel elements presented in Figure 35.

The loads were applied in 6–7 cycles for three fuel elements (tests 4 to 6 in Figure 51). For the remaining two fuel elements, the loads were applied using a single or 2 cycles (tests 7 and 8, respectively, in Figure 51). Because the measurements showed reasonably consistent values between tests, it was concluded that the influence of the number of loading cycles is not an important parameter for the current validation.

The 37-element bundle model was prepared to simulate the fuel element tests by disabling creation of all fuel elements except one from the outer ring. This fuel element was modelled using the model accounting for pellet-to-sheath and pellet-to-pellet interactions described in Section 2.2. Only a part of each endplate adjacent to the simulated fuel pin was preserved in the analysis.

For this analysis the material properties and the design parameters of the 37-element bundle model were set to their nominal values. The sheath thickness was set to the nominal value of 0.42 mm. The axial gap between pellets was set to a constant value of 0.02 mm, as discussed in previous section for the 28-element model. The selection of this value was confirmed through the sensitivity cases presented in the next section.

Simulations of the tests were performed in a similar manner to the 28-element simulations. Zero displacements in all three directions are imposed on the endplate regions that were clamped during the tests. The transversal loads were simulated by applying displacements on the top nodes of the middle bearing pad. These displacements were 2.5, 5, 7.5, 10, 12.5, 15 and 16.5 mm. For each simulated load, the reaction forces in the nodes with imposed displacements were cumulated to obtain the total reaction force. The calculated and measured force vs. displacement responses of the fuel element at the element's center (see Figure 31 for experimental data analysis) are in good agreement, as shown in Figure 51.

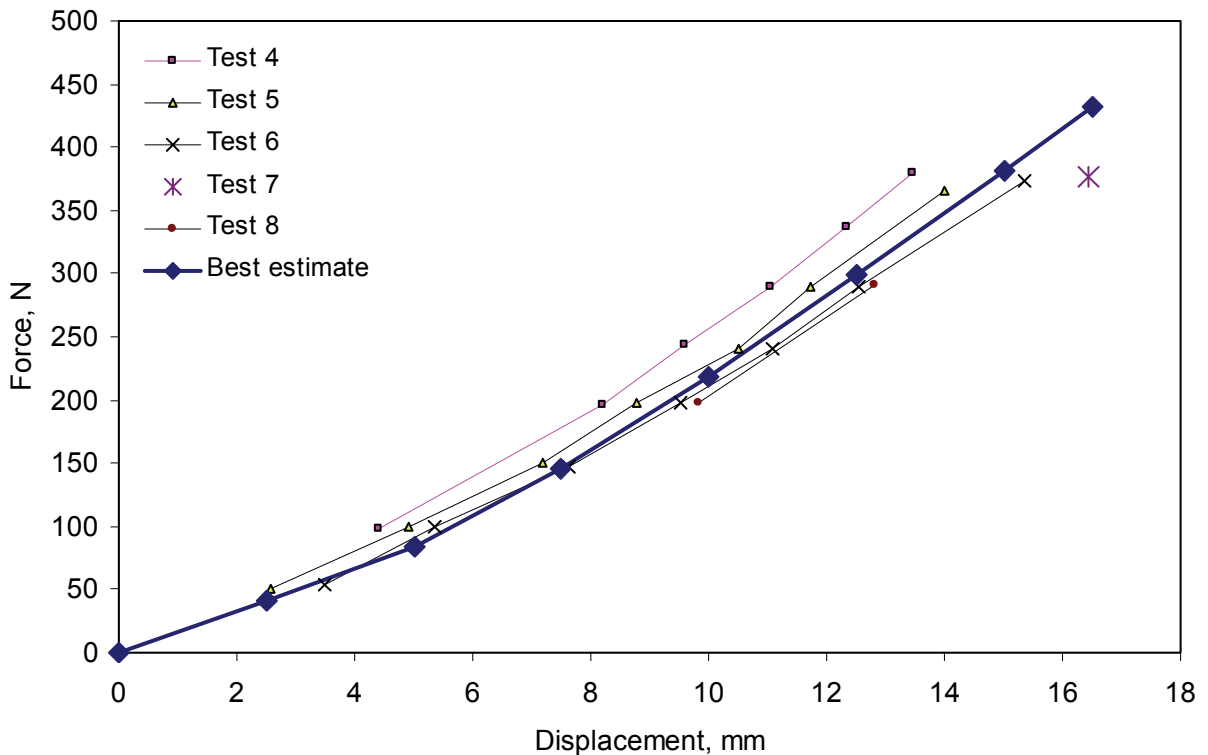


Figure 51: Measured and Modelled Response of a 37-Element Fuel Element

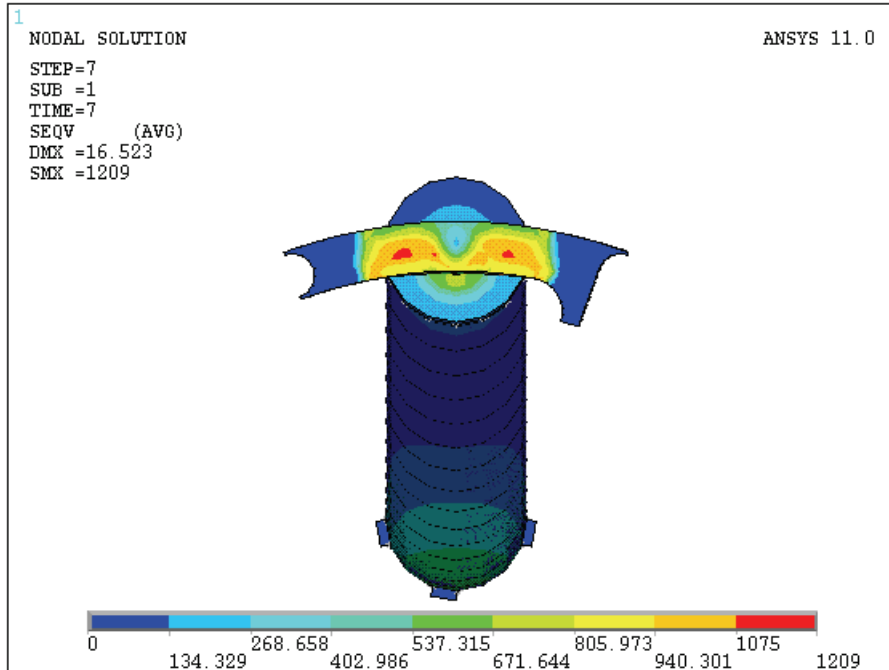


Figure 52: Equivalent Stress in 37-Element Endplate for 16.5 mm Deformation

During the deformation of the fuel elements, the maximum equivalent (Von Mises) stress was obtained in the endplate around the vicinity of the endplate-endcap weld. For 16.5 mm of deflection, the endplate is deformed in the plastic regime presenting a maximum equivalent stress of 1,209 MPa (Figure 52). This is consistent with the permanent deformation seen at higher loads in the tests.

Lower values of the equivalent stress were predicted for the sheath of the fuel element in comparison with the endplate. For the case where a deformation of 16.5 mm was applied, the stress in the sheath was still in the elastic domain, see Figure 53.

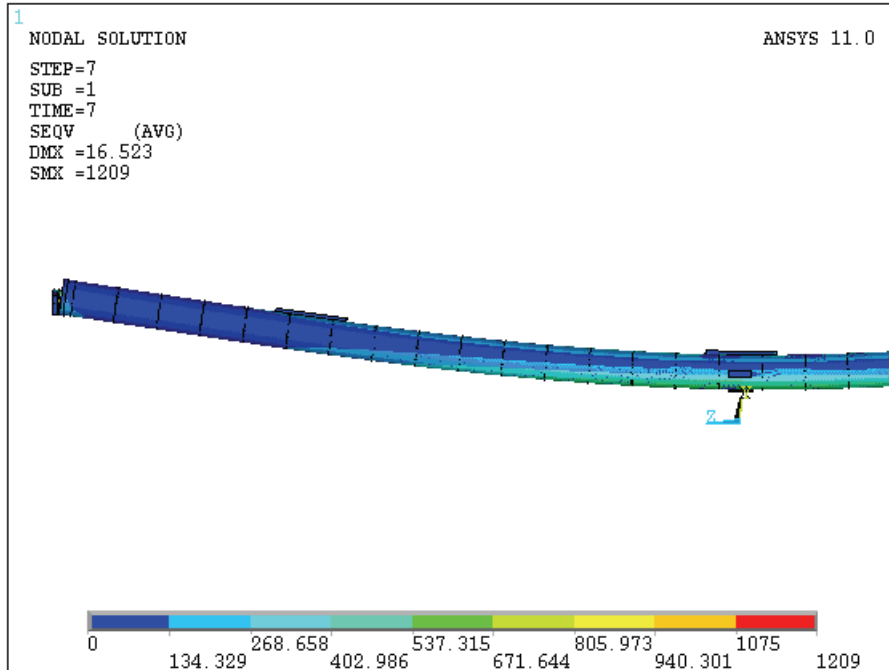


Figure 53: Equivalent Stress in 37-Element Sheath for 16.5 mm Deformation

At higher mechanical deformations, for example at 16.5 mm at the middle of the fuel element, the radial gap is closed for approximately 11 pellets located at the middle of the fuel element. Figure 54 presents the interior surface of the interface finite elements obtained by sectioning the elements with a vertical plane that passes through the fuel element axis of symmetry. The highest interface closure was around -0.04 mm (negative values denote closure) which equals the modelled radial gap. The gap is closed for center-element pellets for all fuel deflections in the range 10–16.5 mm. Approximately 5 pellets located at the fuel element centre interacted with the sheath for the 10 mm deflection case, Figure 55. For a deflection of 7.5 mm, Figure 56, the model predicts that the radial gap is not completely closed for any pellet.

By evaluating the average contact pressure between the pellets and the sheath for the entire fuel element as a function of fuel element deformation it can be noted that for deformations below 7.5 mm the pellet-to-sheath interaction is not significant. At higher fuel deflections the contact pressure presents a steady increase, as seen in Figure 57.

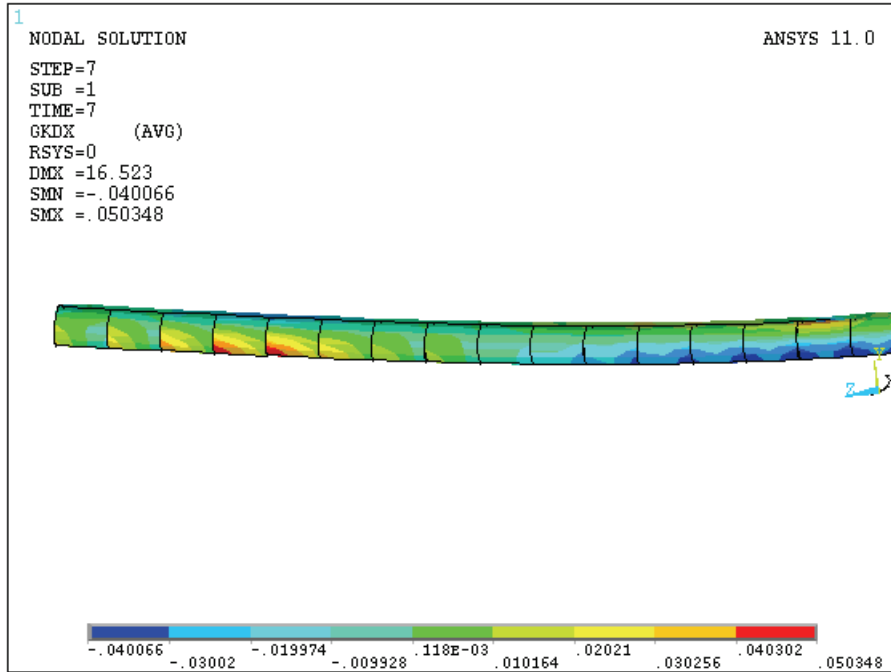


Figure 54: Pellet-to-Sheath Interface Closure for 37-Element Model with 16.5 mm Deformation

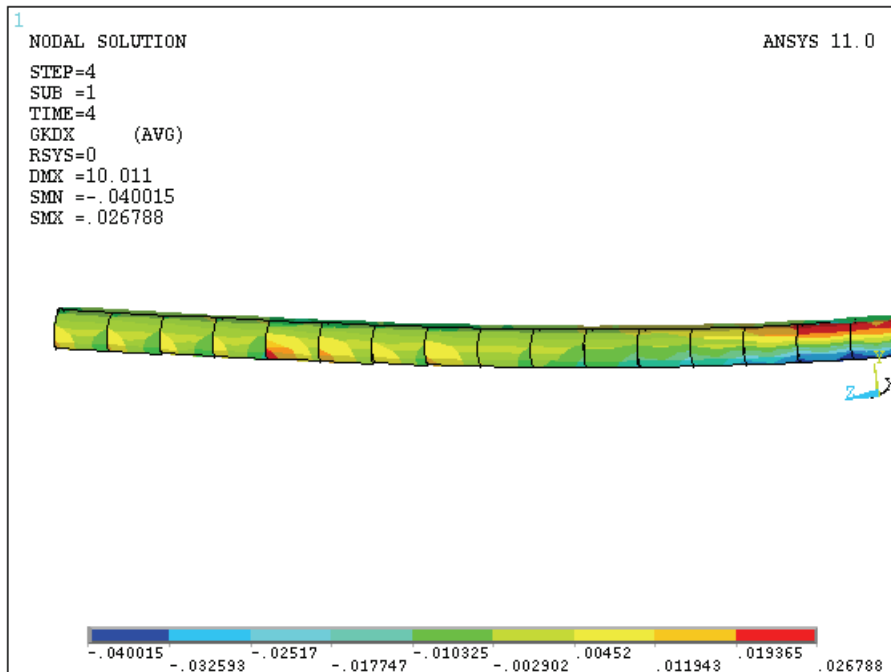


Figure 55: Pellet-to-Sheath Interface Closure for 37-Element Model with 10 mm Deformation

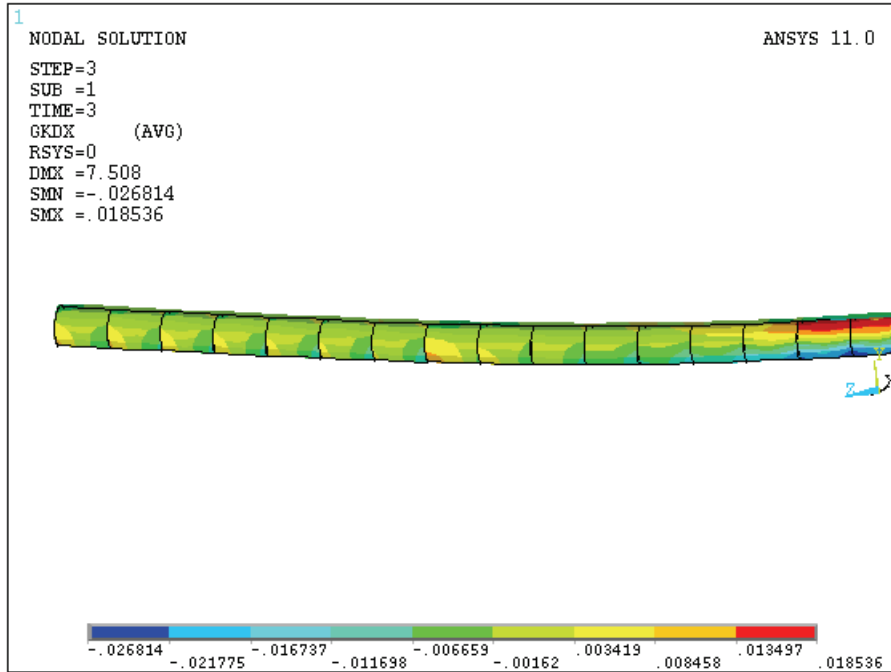


Figure 56: Pellet-to-Sheath Interface Closure for 37-Element Model with 7.5 mm Deformation

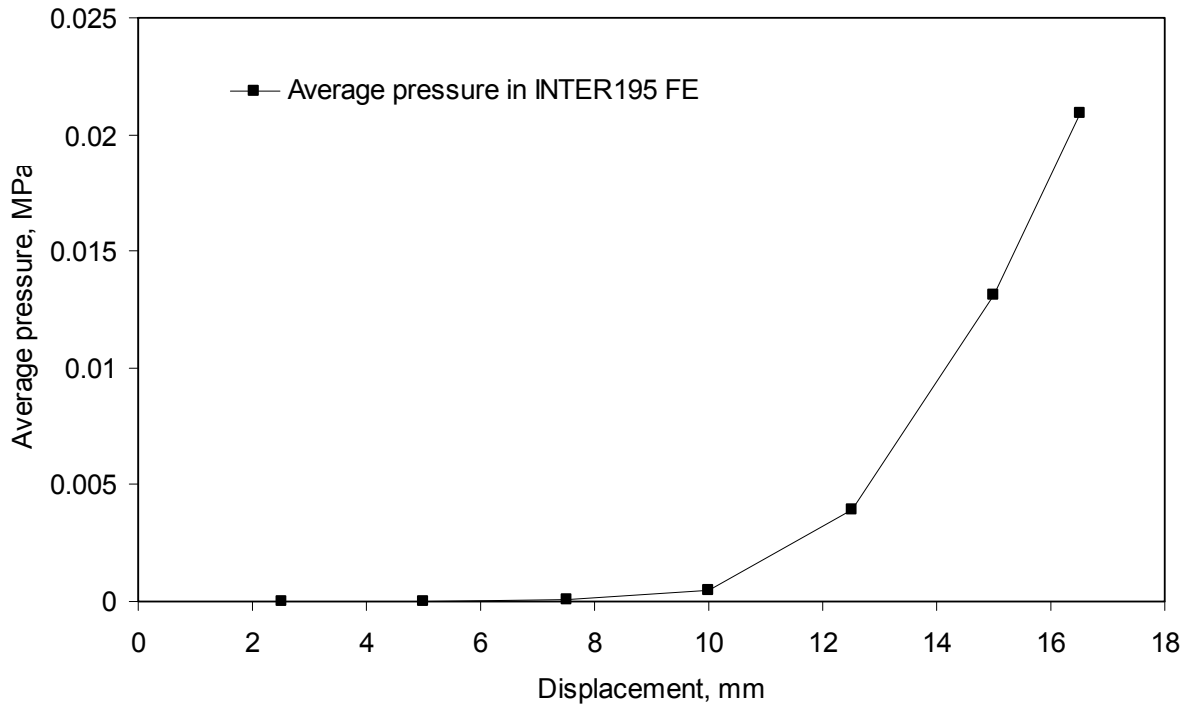


Figure 57: Average Pellet-to-Sheath Pressure vs. 37-Element Deformation

When the radial gap is closed, the pellets contribute to the fuel element's overall stiffness. The Von Mises stress predicted in the pellets for the case of 10 mm deformation is presented in an axial section through the pellets in Figure 58. The high stress values indicate a strong pellet-to-pellet interaction induced by the fuel element bending. This interaction is only significant for the pellets located in the middle of the fuel element. An example of the interaction between adjacent pellets from the central region of the fuel element is presented in Figure 59 for 12.5 mm of deflection (displacements were scaled by a factor of 10).

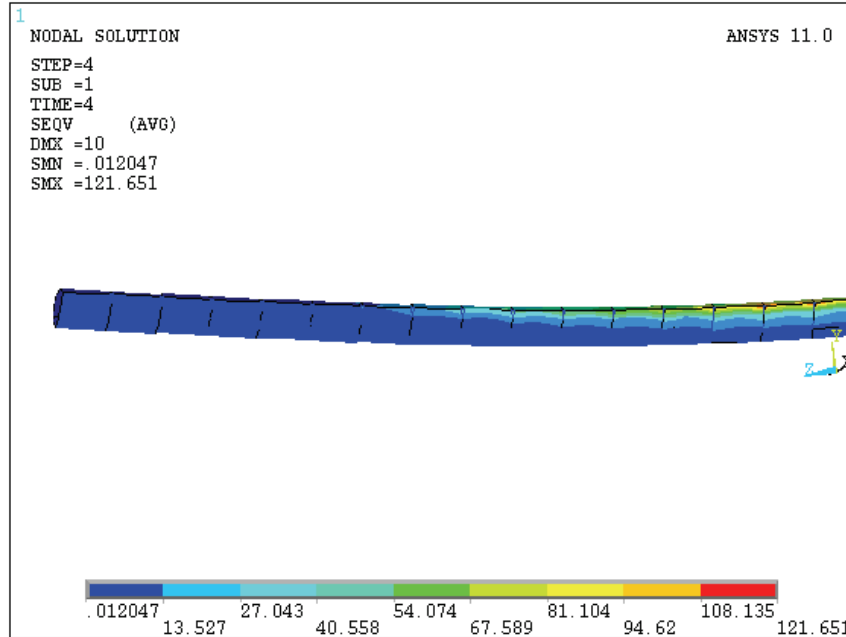


Figure 58: Equivalent Stress in Pellets for 37-Element Model with 10 mm Deformation

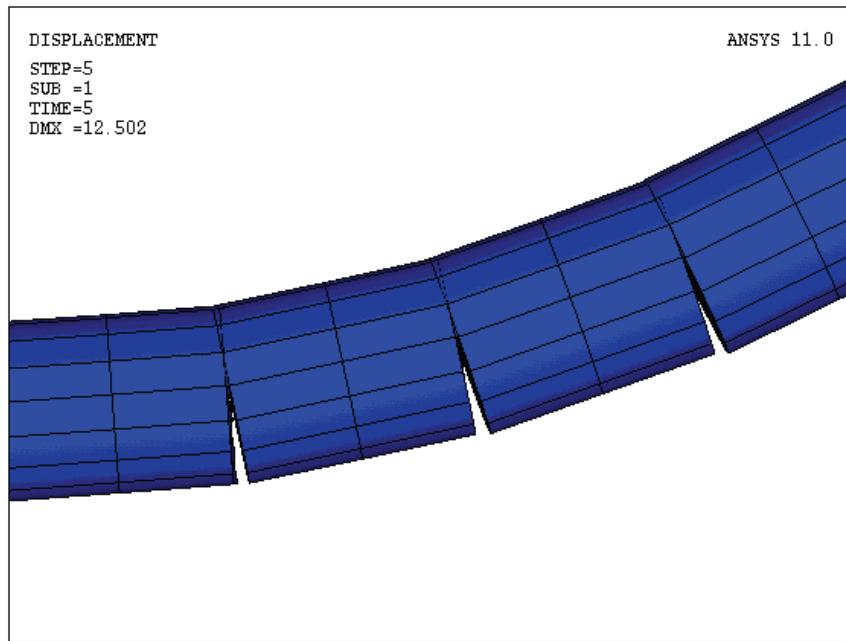


Figure 59: Pellet Interaction for 37-Element Model with 12.5 mm Deformation (10x Scale)

5. UNCERTAINTY AND SENSITIVITY STUDIES

Uncertainty and sensitivity studies were performed to evaluate key parameters affecting the response of the fuel element model to mechanical loads. Analysis of the results of the uncertainty study was also used to evaluate the best estimate values for model parameters that have not been quantified in design documentation or independent studies.

5.1 Uncertainty Parameter List

The parameters identified for the CANDU bundle finite element model uncertainty and sensitivity study were grouped in three categories: material properties, design parameters, and finite element model parameters.

Material property parameters refer to the Zircaloy-4 material properties. UO₂ material properties are neglected in the current study since the elastic modulus for pellets is at least 10 times higher than sheath elastic modulus and, as a result, pellet deformation is not playing a key role in the overall bundle response to the studied mechanical loads. The sensitivity range of the material properties are the uncertainty ranges quoted for the nominal values.

Design parameters are the geometrical parameters used to describe the bundle models. In general, the sensitivity ranges associated to these parameters are the design tolerances.

Model parameters refer to parameters specific to the finite element representation of the bundle model. The uncertainty ranges are based on engineering judgement.

5.1.1 Material properties

5.1.1.1 Young's modulus for the sheath

Young's modulus for zircaloy sheath (E_{sh}) in the alpha phase (at temperatures lower than approximately 1,100 K) is given in MATPRO (MATPRO, 2003) as:

$$E_{sh} = \frac{(1.088 \times 10^{11} - 5.475 \times 10^7 T + K_1 + K_2)}{K_3} \quad (4)$$

where E_{sh} is in Pa, T is the temperature in K, K_1 is a correction to account for the effect of oxidation (Pa), K_2 is a factor to account for the effect of cold work (Pa), and K_3 is a factor to account for the effect of fast neutron fluence.

Because the sensitivity studies will be performed for as-received material, the effect of sheath oxidation and irradiation are not important and $K_2 = 0$ and $K_3 = 1$. Only the cold work effect will be considered for the current bundle model. According to MATPRO (MATPRO, 2003), the equation for the cold work term is:

$$K_2 = -2.6 \times 10^{10} C_{sh} \quad (5)$$

where C_{sh} is the cold work expressed in ratio of areas (unitless).

In MATPRO (MATPRO, 2003) the one sigma uncertainty of Young's modulus for Zircaloy is quoted as 6.4×10^9 Pa. Because the residual values determined from the comparison of the modulus measurements and MATPRO model do not appear to have a common pattern, the distribution of the uncertainty is considered to be normal.

5.1.1.2 Cold work of sheath

The final cold work applied to the sheath reduces Young's modulus according to Equation 4. Most often the cold work is followed by a stress relief thermal treatment. According to measurements presented in MATPRO (MATPRO, 2003), the effect of the stress relief treatment is a reduction of the cold work effect.

The cold work of the Zircaloy-4 sheath used for 28-element and 37-element bundle is a maximum of 15%. Since the magnitude of the stress relief treatment is unknown, the variation of the cold work is considered to be linearly distributed between 0% and the maximum value of 15%.

5.1.1.3 Anisotropy of sheath elastic properties

In many practical applications the anisotropy of the fuel sheath is neglected. The anisotropy is the effect of the strongly textured sheath after the final cold work treatment and is dependent on temperature.

At room temperature the relative changes between elastic modulus in axial, radial, and circumferential directions are not very important. According to MATPRO (MATPRO, 2003), the axial and radial elastic moduli are equal to the isotropic elastic modulus at room temperature. However, the elastic modulus in the circumferential direction is lower than the isotropic modulus by approximately 10^{10} Pa.

Because the texture orientation is not precisely known for the sheath used in 28- and 37-element fuel bundles, it is considered that the effect of anisotropy consists of a reduction of the elastic modulus in the circumferential direction relative to the isotropic elastic modulus. The uncertainty in the circumferential direction is a reduction that is linearly distributed between 0 and 10^{10} Pa. This uncertainty range is valid only for the material properties at room temperature.

5.1.1.4 Poisson's coefficient of sheath

The Poisson ratio is related to Young's modulus and shear modulus as follows:

$$\nu = \frac{E}{2G} - 1 \quad (6)$$

where E is Young's modulus in Pa, and G is the shear modulus in Pa.

According to MATPRO (MATPRO, 2003), the one sigma uncertainty for the Young's modulus model of Zircaloy-4 is 6.4×10^9 Pa. Based only on this value and neglecting the uncertainty of the shear modulus value it is possible to evaluate the uncertainty of the Poisson's ratio. For a temperature of 293.15 K the mechanical properties for as-received Zircaloy-4 with 0% cold work are $E = 9.28 \times 10^{10}$ Pa and $G = 3.40 \times 10^{10}$ Pa. As a result, the corresponding Poisson's

coefficient is 0.362. The one sigma uncertainty of the Poisson's coefficient is 0.094, as determined from the elastic modulus uncertainty.

The value obtained for the uncertainty in Poisson's coefficient is relatively high and is based on indirect measurements. A different set of measured values, reported by Mayoh (Mayoh, 1997), were used to assess the validity of this uncertainty interval. According to Mayoh (Mayoh, 1997), quoting data collected from 4 different experiments performed at room temperature on cold work or annealed zirconium alloys, the minimum and the maximum measured values for Poisson's coefficient are 0.296 and 0.465 respectively. Based on these values, it is recommended to exercise the uncertainty of the Poisson's coefficient in the interval $\pm 1\sigma$.

5.1.1.5 Pre-stress of the fuel bundle

The stress induced in circumferential direction due to the final cold work is partially relieved by a thermal treatment. The value of the non-relieved circumferential stress is not well characterized. In most of the applications, the initial stress is not accounted for because its contribution to the sheath stress and strain can be neglected during irradiation, at high temperature, and high mechanical loads.

Table 3: Material Property Best Estimate Values and Uncertainties

Parameter	Best estimate value	Uncertainty
Young's modulus of sheath E_{sh}	92.8×10^9 Pa (from Equation (4) using a temperature of 293.15 K and a cold work of 0 %)	6.4×10^9 Pa (1 σ , normal distributed)
Cold work for sheath C_{sh}	0 %	0 % – 15 % (Linearly distributed)
Anisotropy of sheath E_{circ}	$E_{circ} = E_{sh}$	From $E_{sh} - 10^{10}$ Pa to E_{sh} (Linearly distributed)
Poisson's coefficient of sheath ν	0.362	0.094 (1 σ , normal distributed in the interval $\pm 1\sigma$)

5.1.2 Bundle design parameters

For most of the design parameters of 28-element and 37-element bundles, the best estimate values were presented in the previous fuel bundle design report (Lampman, 2008). These values were extracted from the Design Description Manuals for 28- and 37-element fuel bundles (Køhn *et al.*, 2002; Køhn *et al.*, 2000).

Because some of the uncertainty ranges have a minor effect on the predictions of the finite element bundle models, only a few parameters will be examined during the sensitivity studies. Based on the anticipated response of the bundle model for pull tests performed on an outer fuel element, the selected parameters for the sensitivity studies are:

- Endplate thickness;
- Endplate outer ring width;

- Pellet diametral clearance⁴ (which will affect the pellet diameter as well);
- Sheath outside diameter; and
- Sheath thickness

The fuel design manual specifies only the minimum value for endplate thickness. For the current study, the best estimate value and uncertainty range were obtained from direct measurements reported by Stern Labs for the experiments (Snell, 2009). The endplate thickness was measured for both endplates of a 28-element bundle and 37-element bundle. From a total of 16 measurements, 6 for the 28-element bundle and 10 for the 37-element bundle, it was computed that the average endplate thickness is 1.78 mm with a standard deviation of 0.04 mm.

Table 4: Design Parameters Best Estimate Values and Uncertainties

Parameter name	28-element bundle		37-element bundle	
	Best estimate value	Uncertainty (tolerance)	Best estimate value	Uncertainty (tolerance)
Endplate thickness ^(a)	1.78 mm	Normal distributed, 1 σ = 0.04 mm	1.78 mm	Normal distributed, 1 σ = 0.04 mm
Endplate outer ring width	5.05 mm	Linearly distributed in the interval [4.9,5.2] mm	4.5 mm	Linearly distributed in the interval [4.3,4.7] mm
Pellet diametral clearance	0.08 mm	Linearly distributed in the interval [0.03,0.13] mm	0.08 mm	Linearly distributed in the interval [0.03,0.15] mm
Sheath outside diameter	15.25 mm ^(b)	Linearly distributed in the interval [15.18,15.32] mm	13.08 mm ^(b)	Linearly distributed in the interval [12.99,13.12] mm
Sheath thickness	0.425 mm ^(c)	Linearly distributed in the interval [0.38,0.47] mm	0.41 mm ^(c)	Linearly distributed in the interval [0.38,0.457] mm

Notes:

a) Based on measurements of the endplate thickness.

b) The ovality of the sheath is not accounted for. See for example AECL-TS-XX-37354-001 Rev 1, "Zirconium Alloy Seamless Tubing for Reactor Fuel Sheathing" (1989).

c) Evaluated based on tolerance limits.

⁴ The diametral clearance is defined as twice the radial gap.

5.1.3 Other model parameters

In addition to the material properties and design parameters, a supplementary set of modelling parameters needs to be studied as part of sensitivity studies. Such parameters are intrinsic to the finite element model and to the computer code, ANSYS, used to solve the numerical problem of the stress and strain distribution.

5.1.3.1 Finite element sizes

The mesh size is an important parameter that can affect the prediction accuracy of the finite element model. To check the effect the mesh sizing has on the response of the fuel element, several simulations with different axial and circumferential mesh sizes were run.

5.1.3.2 Pellet-to-sheath interaction

In the current model, the interaction between the sheath and pellets is modelled using a specialized type of finite element for interfaces. This finite element links the pellet surface and inner surface of the sheath in order to model the radial gap status. A user-specified material property is used to transfer pressure between the contact surfaces. The pressure transfer function is an important model parameter that has the role of smoothing the response of the contact during the transition between the two possible states. The effect that the pressure transfer function has on the simulated results should be evaluated to confirm the suitability of the transfer function employed in the model.

5.2 Analysis Methodology

The methodology used to evaluate the influence of the uncertainty parameters to the model predictions is based on ordered statistics, namely the GRS method (Glaeser, 2000). This methodology is largely used in the nuclear industry, especially for accident analyses and for realistic simulation of normal operating conditions.

The GRS approach consists of preparing a case matrix containing N cases for which the model uncertainties are randomly sampled from their distributions. The number of cases, N , depends on the statistical statement required at the end of analyses and the associated confidence level for the statement. The most common output of the GRS methodology is a range of values that cover 95% of cases with a 95% confidence level, referred to as 95/95 interval.

The number of cases, N , is determined using the following inequality (Somerville, 1958) determined by order statistics of a sample from a population with a continuous but unknown distribution function:

$$\gamma \leq I_{1-P}(m, N - m + 1) \quad (7)$$

where γ is the confidence level, I is the incomplete Beta function, P is the fraction of the population that lies between r^{th} smallest and s^{th} largest of the sample, and $m = r + s$. The inequality is applicable to any particular choice of r and s . For one-sided confidence intervals either $r = 0$ or $s = 0$. For a double sided interval r and s are greater than 0.

The equation for the incomplete Beta function is:

$$I_x(a, b) = \sum_{j=a}^{a+b-1} \frac{(a+b-1)!}{j!(a+b-1-j)!} x^j (1-x)^{a+b-1-j} \quad (8)$$

The confidence level to have 95% of the population ($P=0.95$) between 1st minimum and 1st maximum of all samples as a function of number of samples is listed in the following table.

Table 5: Confidence Level as a Function of Number of Samples to have 95% of the Population between First Minimum and First Maximum of All Samples

Number of samples	Confidence level	
90	0.9433	
91	0.9456	
92	0.9479	
93	0.9500	≥ 95% confidence
94	0.9521	
95	0.9541	
96	0.9560	
97	0.9578	
98	0.9596	
99	0.9613	≥ 96% confidence
100	0.9629	
101	0.9645	
102	0.9660	
103	0.9674	
104	0.9688	
105	0.9701	≥ 97% confidence

5.3 Uncertainty Analysis for 28-Element Bundle Model

The cumulated effect of the uncertainty parameters identified in section 5.1 is studied with the GRS methodology. The uncertainty analysis is performed for the 28-element fuel bundle model applied to simulate the non-axial loading tests performed on a fuel element. The main output of the finite element simulation is the reaction force predicted for displacements imposed at the fuel element middle. This can be directly compared with the measurements.

The uncertainty parameters are sampled randomly using their distributions. For parameters having unknown distributions, a linear distribution was assumed. This assumption is conservative since it will maximize the influence of such parameters over the model uncertainty. According to the ordered statistics, the maximum and minimum predicted values from a number of 93 cases will cover 95% of the population with a 95% confidence level.

The list of uncertainty parameters and their distribution used for the case matrix is presented in Table 6. The first parameter, the material property used for pressure response of the pellet-to-sheath interface, should not influence the results. This assumption remains to be confirmed as part of this study.

The effect of the sheath cold work and anisotropy was not explicitly accounted for. These sources of uncertainties will be covered by the uncertainty in Young's modulus and the Poisson coefficient. For both parameters, their normal distribution was not limited to maximum/minimum values and their values in the case matrix can vary unrestricted.

The interval for the variation of the axial gap was selected between 0 mm and 0.04 mm. Based on preliminary analyses, it was discovered that there will be no pellet-to-pellet interactions if a uniform axial gap of 0.04 mm is applied. The total axial gap corresponding to the maximum value is approximately 1.3 mm.

The results obtained for the case matrix are presented in Figure 60 together with the predictions for the best estimate case as well as the experimental measurements.

Table 6: Best Estimate Values and Uncertainty used for 28-Element Bundle Sensitivity Analyses

Parameter	Best estimate value	Uncertainty
1. Material property for pellet-to-sheath interface. Value of the contact pressure for the first point of the interface closure (located at 0.005 mm)	100 MPa	Linear distributed minimum = 0.5 MPa maximum = 150 MPa
2. Shear modulus for pellet-to-sheath interface.	1.5 MPa	Linear distributed minimum = 0.005 MPa maximum = 8 MPa
3. Pellet-to-pellet axial gap	0.02 mm	Linear distributed minimum = 0 mm maximum = 0.04 mm
4. Pellet-to-sheath radial gap	0.04 mm	Linear distributed minimum = 0.01 mm maximum = 0.05 mm
5. Zircaloy-4 elastic modulus	92.8×10^9 Pa	Normal distribution $\mu = 92.8 \times 10^9$ Pa $\sigma = 6.4 \times 10^9$ Pa
6. Zircaloy-4 Poisson coefficient	0.362	Normal distribution $\mu = 0.362$ $\sigma = 0.094$
7. Endplate thickness	1.78 mm	Normal distribution $\mu = 1.78$ mm $\sigma = 0.04$ mm
8. Endplate outer ring width	5.05 mm	Linear distributed minimum = 4.9 mm maximum = 5.2 mm
9. Sheath thickness	0.45 mm	Linear distributed minimum = 0.38 mm maximum = 0.47 mm

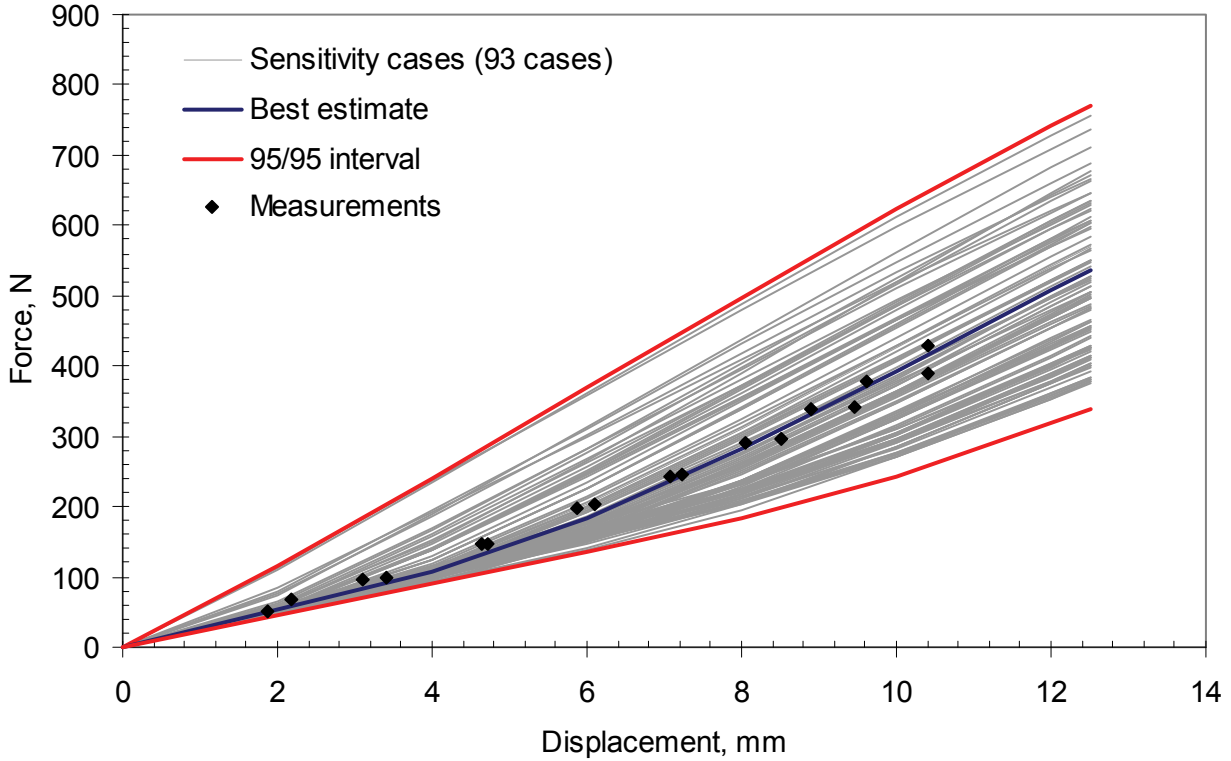


Figure 60: 28-Element Bundle Model Predictions for GRS Matrix Cases

The 95/95 upper limit shows very large values for the reaction force when compared with the experimental data or with the best estimate case. During analysis of the cases that lead to such high predictions for the reaction forces it was noted that these cases present an axial gap of approximately zero. For such conditions, the pellet stack added a large stiffness to the model even at low deformations.

The most influential parameter for the 28-element bundle model is the pellet-to-pellet axial gap. In the region of large displacements, 10 mm in Figure 61, the model predictions are strongly influenced by the axial gap across the entire uncertainty interval, from 0 mm to 0.04 mm.

For low deformation, 2 mm or 4 mm applied at the centre of the fuel element, the predicted reaction forces depend on the axial distance between pellets only for low values of the gap, Figure 61. Once the axial gap between pellets exceeds the contact value it does not influence the results. In this region, analysis of the sensitivity results indicates that the response is dependent on the Young's modulus of the Zircaloy-4 sheath. Figure 62 presents the reaction for the 2 mm deflection case as a function of the sheath elastic modulus. The relative elastic modulus presented in the figure is the ratio of the sensitivity case elastic modulus relative to the best estimate elastic modulus.

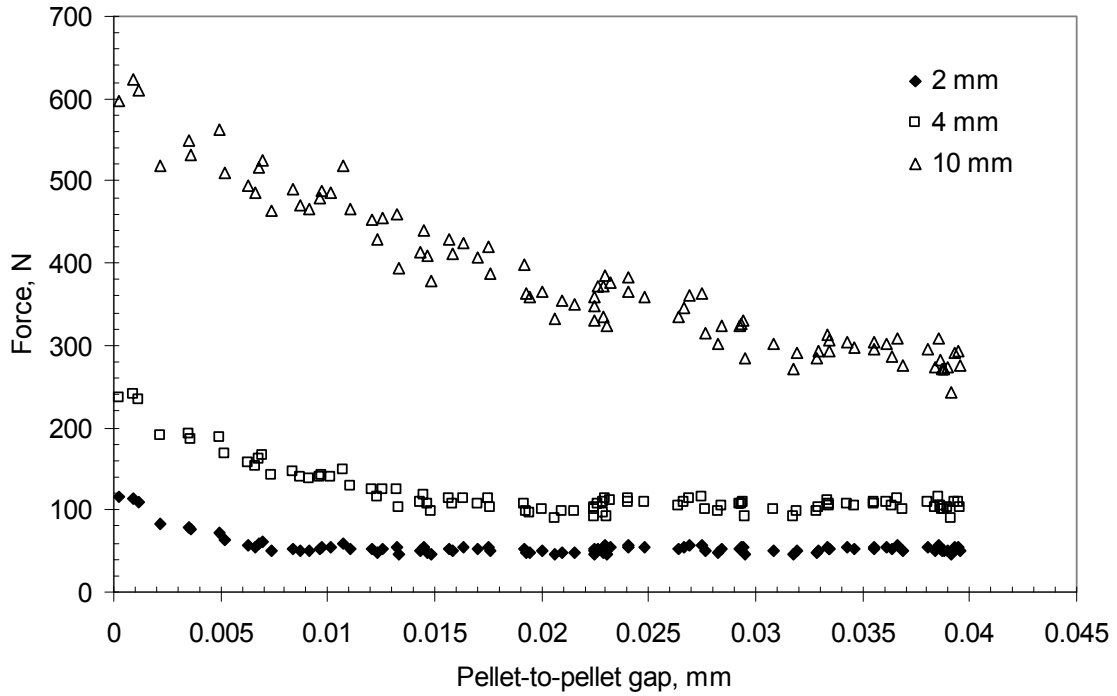


Figure 61: Influence of the Pellet-to-Pellet Axial Gap on the 28-Element Fuel Bundle Model Predictions

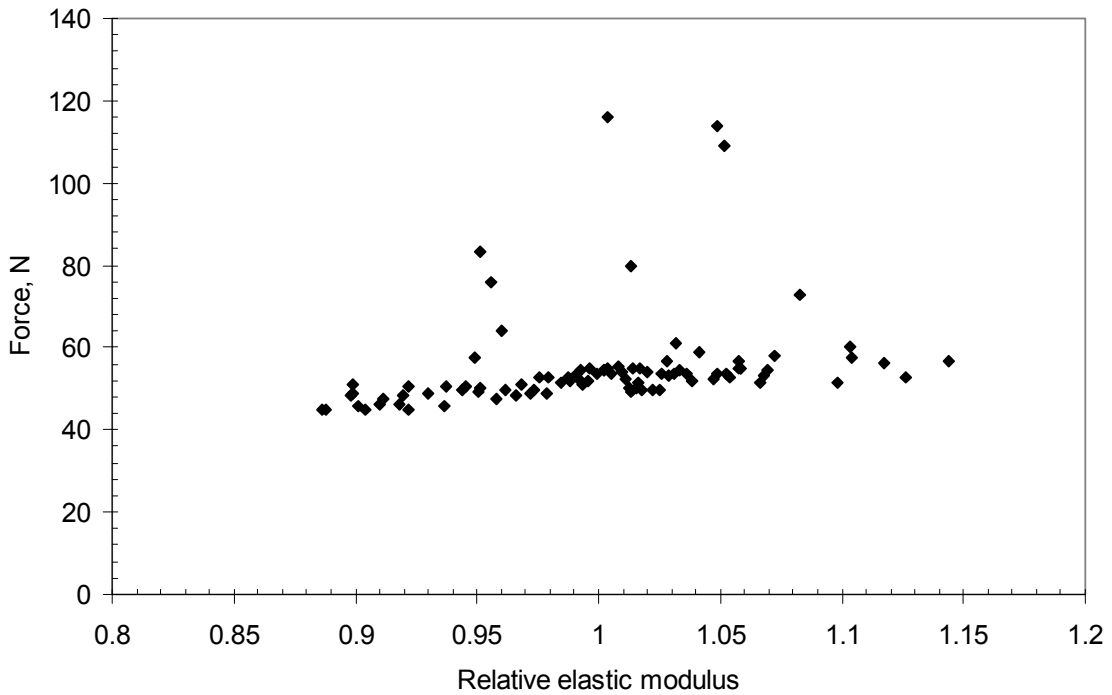


Figure 62: Influence of the Zircaloy-4 Elastic Modulus on the 28-Element Fuel Bundle Model Predictions for 2 mm Load Case

For the best estimate case, it was noted that for an applied displacement of 8 mm the radial gap between pellets and sheath is closed for a few central pellets. For a deflection of 6 mm at the centre of the fuel element, the model predicts that a small radial gap still exists. According to these results, we can assume that the pellets located at the middle of the fuel element are moving inside the fuel sheath up to the radial gap closure, which appears between 6 and 8 mm lateral deflection of the fuel. So, an axial interaction between the pellets in the interval of non-axial loads from 0 to 6 mm will produce movement of the pellets rather than a strong pellet-to-pellet interaction. In other words, pellet relocation is possible up to radial gap closure at non-axial loads in excess of 6 mm.

The sensitivity study for the case with 6 mm deflection reveals that the axial gap between pellets has a strong influence on the results for situations when the axial gap is below 0.02 – 0.025 mm, shown in Figure 63. Assuming that the pellets are relocating, because the radial gap is still open for the considered fuel deformation, we can conclude that the most realistic value of the axial gap between the pellets of the as-received bundle is 0.02 – 0.025 mm. For higher deflections of the fuel element, which will cause the closure of the radial gap and suppress the pellets' movements relative to the sheath, the axial gap between the pellets will remain unmodified.

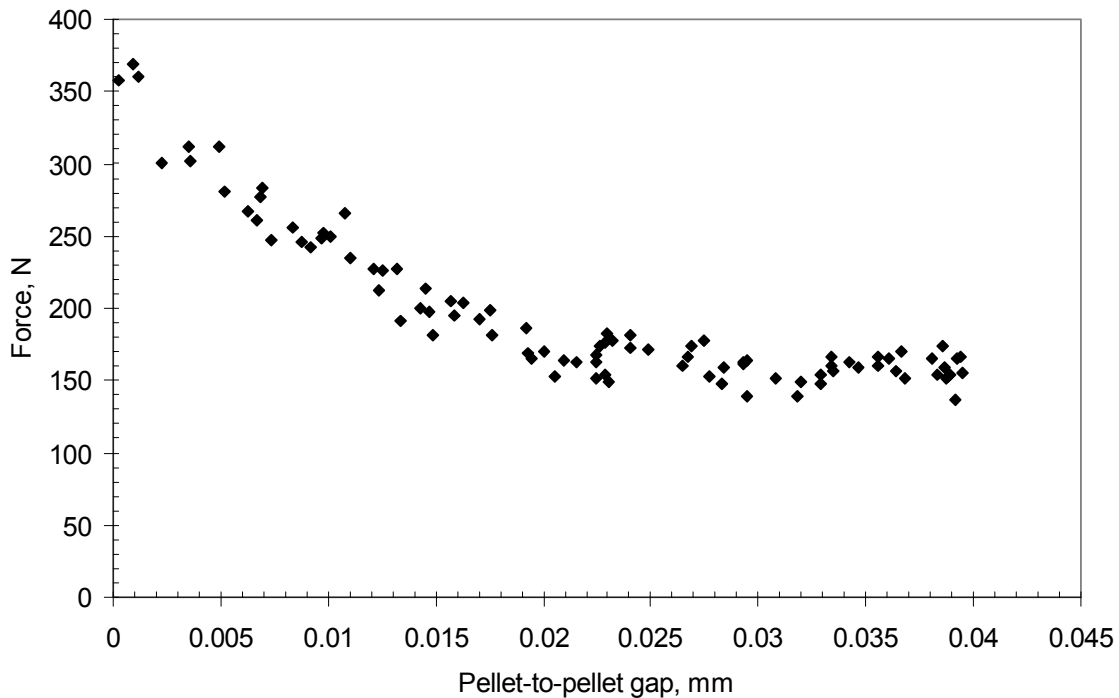


Figure 63: Influence of the Pellet-to-Pellet Axial Gap on the 28-Element Fuel Bundle Model Predictions for 6 mm Load Case

5.4 28-Element Model Sensitivity to Axial Size of the Finite Elements

The size of the finite elements used to model the sheath, pellets, and pellet-to-sheath interface was modified in axial direction to examine the effect. By default, the 28-element bundle model uses an axial length of the finite elements equal with the half of the pellet length. The number of

finite elements was increased from 2 per pellet length to 10 per pellet length, as shown in Figure 64. The results obtained for the reaction forces as a function of applied deformation show acceptable consistency results between the default mesh and the finer mesh (Figure 65).

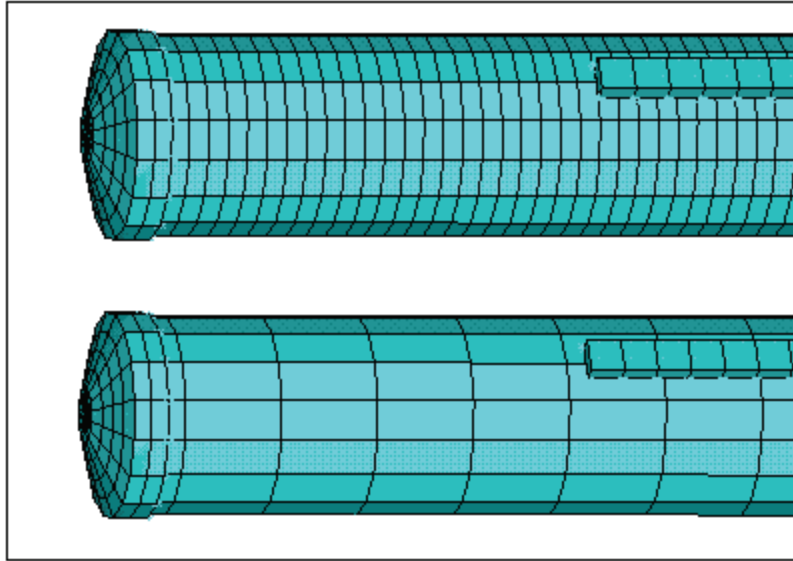


Figure 64: Comparison of Sheath Mesh for Axial Mesh Size Sensitivity Analysis

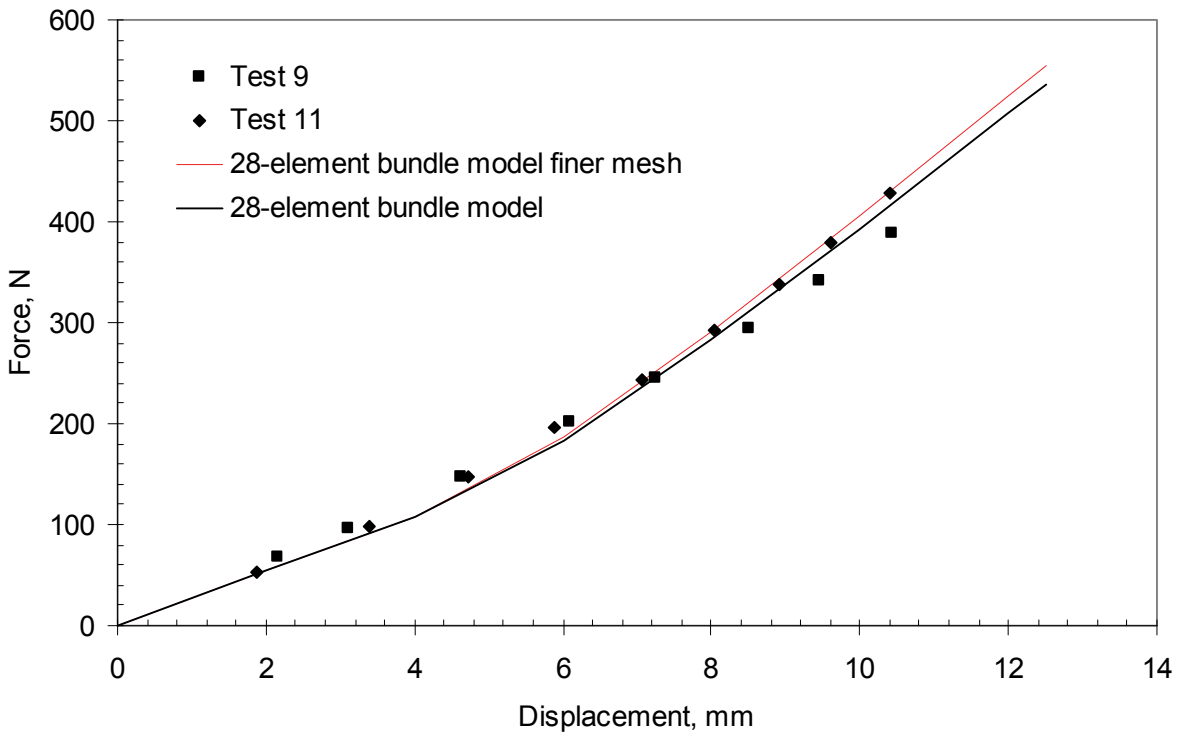


Figure 65: Results of Axial Mesh Size Sensitivity Study

5.5 Uncertainty Analysis for 37-Element Bundle Model

As in the 28-element sensitivity study, the cumulated effect of the uncertainty parameters identified in Section 5.1 is studied for the 37-element model using the GRS methodology. This sensitivity analysis is performed for the 37-element fuel bundle model applied to simulate the non-axial loading tests performed on a fuel element. The main output of the finite element simulation are the reaction forces predicted for displacements imposed at the fuel element middle, which can be directly compared with the measurements.

A number of 93 cases were executed and the minimum and maximum values will cover over 95% of the reaction force population with a 95% confidence level. For each sensitivity case, the uncertainty input parameters are sampled randomly according to their distribution. The uncertainty parameters used for the case matrix are presented in Table 7.

The interval for the variation of the axial gap was selected between 0 mm and 0.04 mm. Based on preliminary analyses, it was discovered that there will be no pellet-to-pellet interactions if a uniform axial gap of 0.04 mm is applied. The total axial gap corresponding to the maximum value is approximately 1.3 mm.

The results of the sensitivity studies are presented in Figure 66 together with the force/displacement measurements. The experimental data are between minimum and maximum predictions, which represent the 95/95 limits obtained from the uncertainty analysis.

The upper limit shows large values for the reaction force when compared with the experimental data or with the best estimate case. During evaluation of the cases that lead to such high predictions for the reaction forces, it was noted that these cases present an axial gap of approximately zero. For such conditions, the pellet stack added a large stiffness to the model even at low deformations.

For low deflections, 2.5, 5 or 7.5 mm applied at the centre of the fuel element, the predicted reaction forces depend on the axial distance between pellets. This is especially true for low values of the gap, Figure 67. Once the axial gap between pellets exceeds the contact value the influence on the results became negligible.

For a 10 mm lateral deflection the radial gap closes for the pellets located at the fuel element centre and suppresses their relocation. Up to this deflection the pellets can move axially inside cladding and the pellet-to-pellet distance can readjust. Once the radial gap is closed, at 10 mm deflection of the fuel element, the axial distance between pellets will no longer be subjected to changes. For this reason, the axial distance set due to the pellet relocation at previous load step, 7.5 mm deflection, is considered to remain constant throughout further deflections. According to the predictions presented in Figure 67 for the 7.5 mm deflection case, the minimum axial gap size for which the pellet-to-sheath interaction is not activated is 0.02 – 0.025 mm. A fixed lower value of the initial axial gap will induce strong interaction between pellets, as can be seen from the high reaction forces, but in reality the pellets will relocate since the radial gap is not constraining the axial movement of the pellets.

Table 7: Best Estimate Values and Uncertainties used for 37-Element Bundle Sensitivity Analyses

Parameter	Best estimate value	Uncertainty
1. Material property for pellet-to-sheath interface. Value of the contact pressure for the first point of the interface closure (located at 0.005 mm)	100 MPa	Linear distributed minimum = 0.5 MPa maximum = 150 MPa
2. Shear modulus for pellet-to-sheath interface.	1.5 MPa	Linear distributed minimum = 0.005 MPa maximum = 8 MPa
3. Pellet-to-pellet axial gap	0.02 mm	Linear distributed minimum = 0 mm maximum = 0.04 mm
4. Pellet-to-sheath radial gap	0.04 mm	Linear distributed minimum = 0.01 mm maximum = 0.07 mm
5. Zircaloy-4 elastic modulus	92.8×10^9 Pa	Normal distribution $\mu = 92.8 \times 10^9$ Pa $\sigma = 6.4 \times 10^9$ Pa
6. Zircaloy-4 Poisson coefficient	0.362	Normal distribution $\mu = 0.362$ $\sigma = 0.094$
7. Endplate thickness	1.78 mm	Normal distribution $\mu = 1.78$ mm $\sigma = 0.04$ mm
8. Endplate outer ring width	5.05 mm	Linear distributed minimum = 4.9 mm maximum = 5.2 mm
9. Sheath thickness	0.42 mm	Linear distributed minimum = 0.38 mm maximum = 0.46 mm

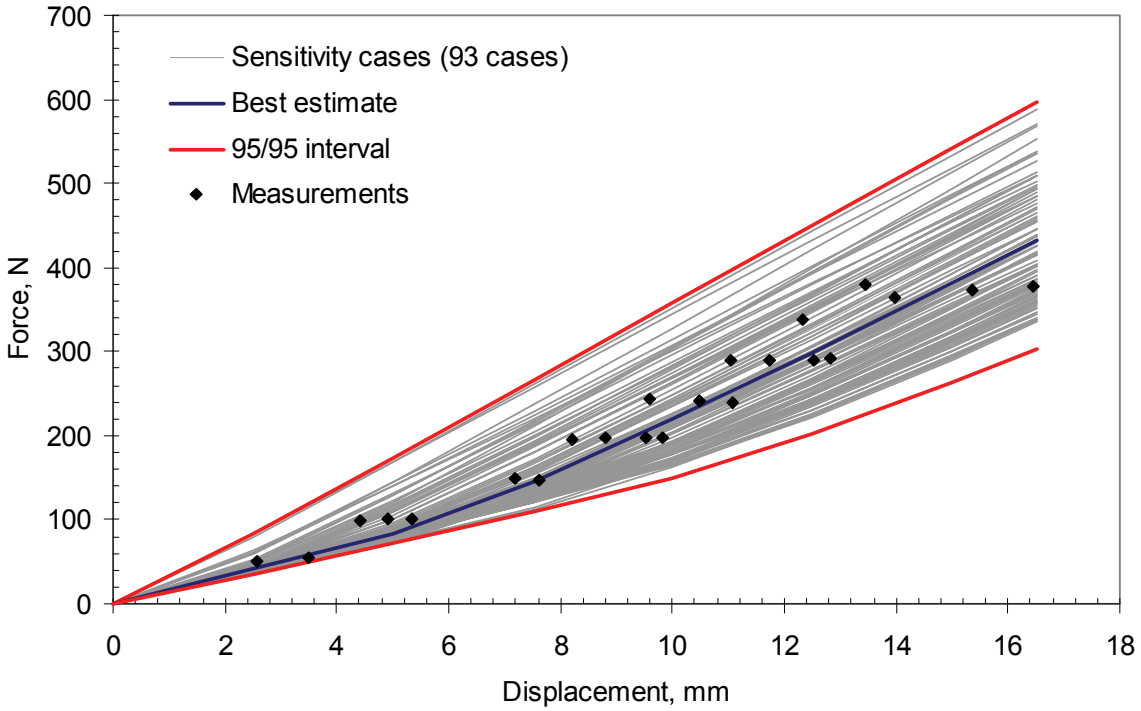


Figure 66: 37-Element Bundle Model Predictions for GRS Sensitivity Cases

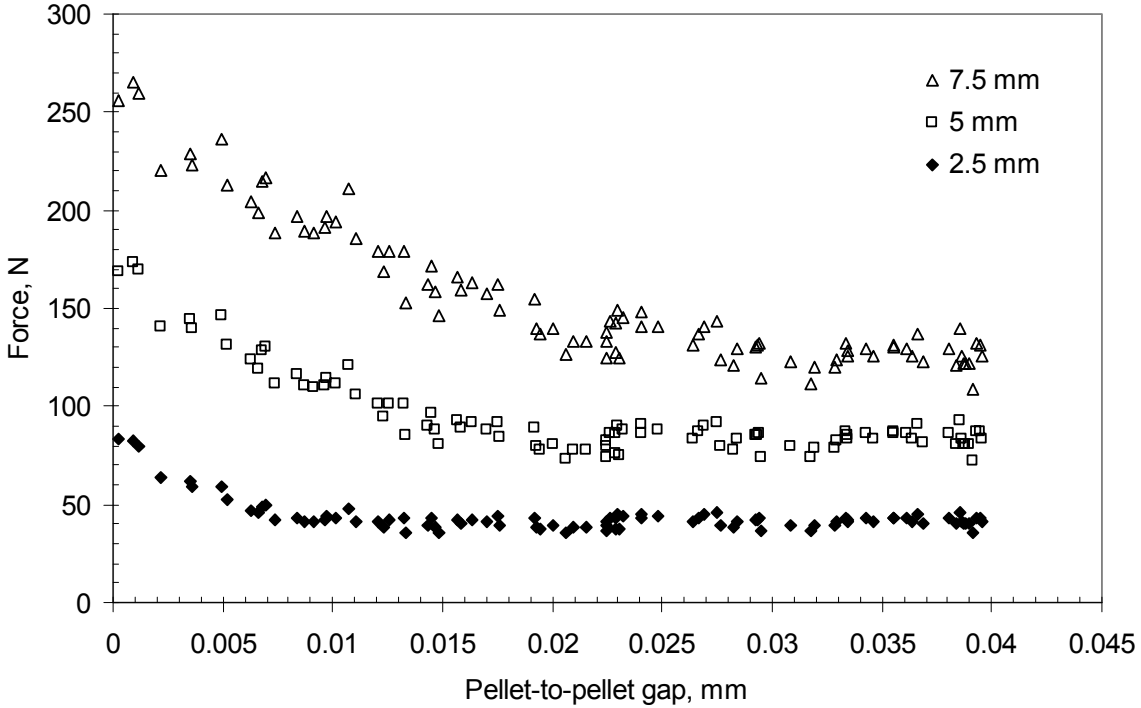


Figure 67: Influence of the Pellet-to-Pellet Axial Gap on the 37-Element Fuel Bundle Model Predictions

At lower values of the lateral deflections, the axial gap between pellets is not playing a very important role. From the sensitivity studies it was observed that in this range of low mechanical deformation the most influential parameter is the elastic modulus of the Zircaloy-4 (Figure 68).

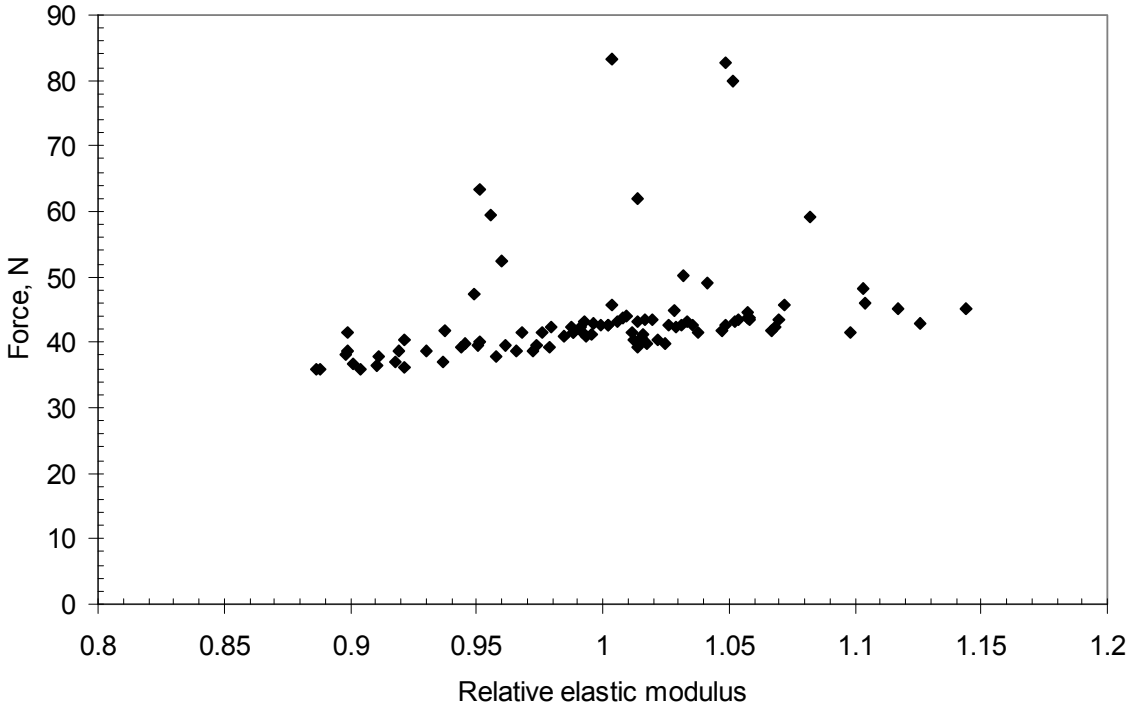


Figure 68: Influence of the Zircaloy-4 Elastic Modulus on the 37-Element Fuel Bundle Model Predictions for 2.5 mm Deflection Case

5.6 Bundle Model Sensitivity to Circumferential Size of the Finite Elements

By default, the 28-element and 37-element bundle models are using 16 finite elements to mesh the sheath and the pellets in circumferential direction. The number of finite elements was increased to 32 along the circumference for the 37-element bundle to study the influence of the mesh size on the model predictions. The axial mesh size was not altered. The fine mesh is presented in Figure 69. The predicted reaction forces as a function of fuel element deflection shows consistent results between the default and the finer mesh, Figure 70.

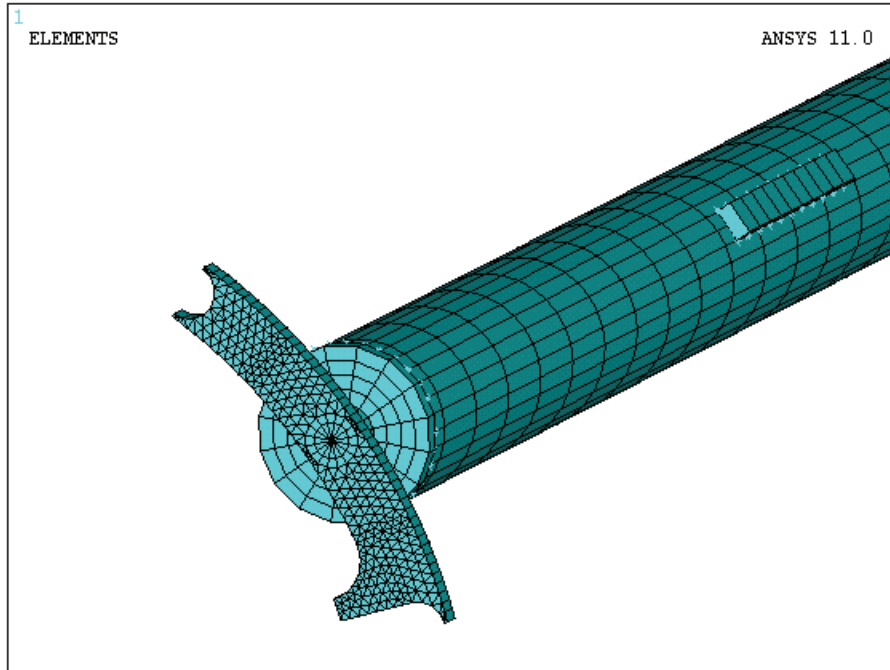


Figure 69: Sensitivity Study for Finer Mesh in Circumferential Direction

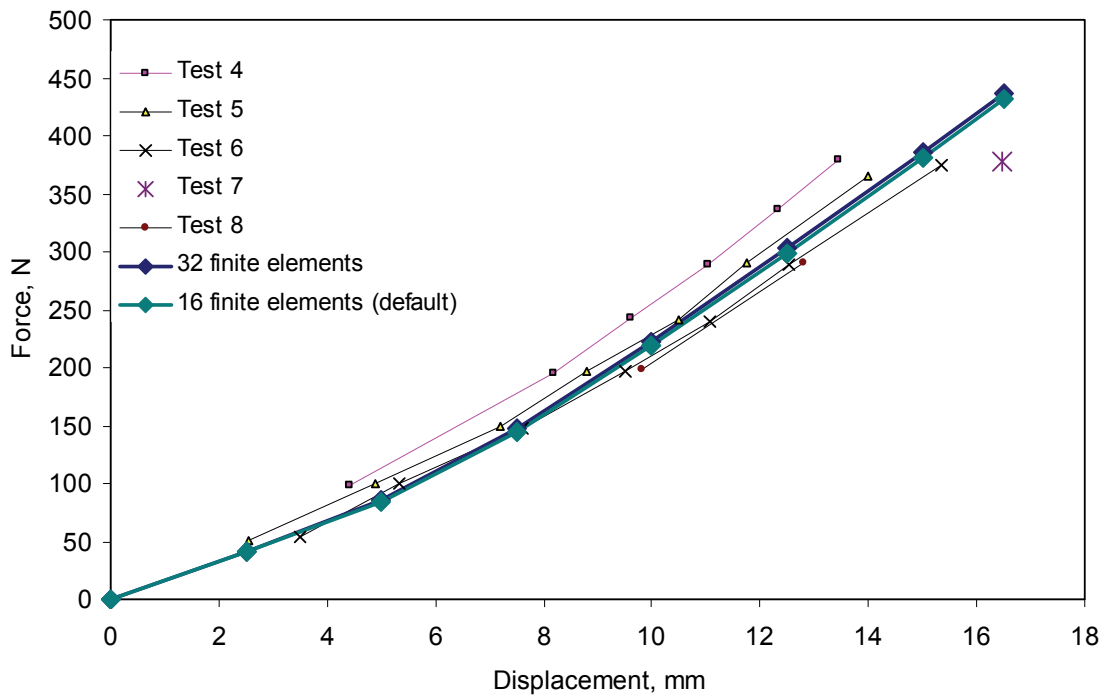


Figure 70: Sensitivity Study for the Circumferential Size of Finite Elements

6. CONCLUSIONS

New models have been created for the fuel elements with improved modelling of the pellet-to-sheath and pellet-to-pellet interactions. A new series of tests on single fuel elements were performed and showed a similar fuel element response to the full-bundle tests. Validation of the experimental apparatus using a solid rod showed good consistency in the experimental results between tests. This indicates that variations in response of the fuel elements seen between different tests from the same series are not a result of the experimental apparatus, but likely due to the fuel elements themselves.

The new models for the 28- and 37-element bundles were applied to simulate the recent validation tests performed at Stern Labs using single fuel elements. The results obtained for the best estimate case of both models are in good agreement with the measurements. The predicted stresses and strains and the interaction between pellets and sheath or between pellets appear to be consistent with the expected behaviour and range of values.

An uncertainty analysis was performed by varying the model input parameters in their allowable ranges. The uncertainty studies revealed that the 28- and 37-element bundle models are capable of simulating the mechanical behaviour of the bundle for different combinations of the uncertain parameters. The most important parameters for the model predictions are the axial gap between pellets, followed by the elastic modulus of the sheath and sheath thickness. The best-estimate value for the axial gap between pellets was justified based on an analysis of the results from the sensitivity cases. The self-adjusting capability of the axial gap between the pellets in relation to the closure of the radial gap between pellets and sheath during the non-axial loads is the key factor in the selection of the best estimate value of the pellet-to-pellet gap.

7. REFERENCES

- Glaeser, G. 2000. Uncertainty evaluation of thermal-hydraulic code results. International Meeting on "Best Estimate" Methods in Nuclear Installation Safety Analysis (BE-2000). Washington DC, USA.
- Køhn, E. *et al.* 2000. Design description and operational limits: 37-element fuel bundle. OPG Document N-DDD-37000-10000-R00. Toronto, Ontario.
- Køhn, E. *et al.* 2002. Design description and operational limits: 28-element fuel bundle. OPG Document P-DD-37000-10001-R00. Toronto, Ontario.
- Lampman, T. and Daniels, T. 2005. Proposed tests and examinations to provide assurance of fuel integrity during dry storage and subsequent handling. NSS Report P0499/RP/001 R01. Toronto, Ontario.
- Lampman, T. 2008. CANDU fuel bundle stress model for used fuel dry storage analysis. Nuclear Waste Management Organization. AMEC NSS Report NW007/RP/001 R00. Toronto, Ontario
- MATPRO 2003. 2003. SCADAP/RELAP5-3D code manual volume 4: MATPRO – a library of materials properties for light-water-reactor accident analysis. INEEL/EXT-02-00589, Volume 4, Revision 2.2.
- Mayoh, K.R. 1997. A compendium of material properties for zirconium alloy. CANDU Owners Group Report COG-96-101. Toronto, Ontario.
- Pilkey, W.D. 1994. Formulas for stress, strain, and structural matrices. John Wiley & Sons, Inc.
- Snell, J. 2009. Mechanical deformation tests on 37 and 28 element fuel elements. Stern Laboratories Incorporated Report SL-205. Hamilton, Ontario.
- Somerville, P.N. 1958. Tables for obtaining non-parametric tolerance limits. The Annals of Mathematical Statistics, 1958; 29: 599-601.